

## Final Author Comments

Below we copy our original responses previously posted as interactive comments in black text. The red text details the changes that have been made to the manuscript. There were a few additional minor editorial changes (please see the marked up manuscript, appended to this response, for details) and two more significant changes.

1. We revised Figure 1, which had the wrong y-axis labels.
2. We removed reference to Daley (1991), which was not referenced in the manuscript.

## Response to Referee 1

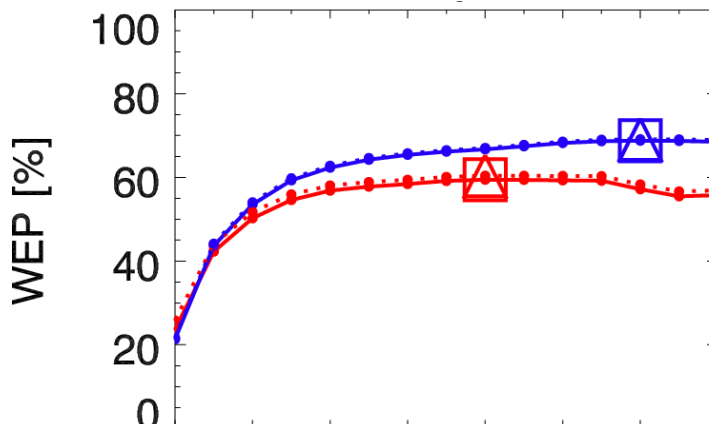
*1) Regarding the "perturbed-observation" EnKF methodology, it is not clear how the data are assimilated. Specifically, at a given assimilation step, are all observations assimilated at once or are observations assimilated sequentially by batches ?*

The ozone and height observations are assimilated together in a single batch for each assimilation step. We will make this point clear in the revised version.

A sentence was added in Section 2.2 to address this point.

*2) In the height-only assimilation experiment, looking at Fig. 9, the optimal localization length seems to be beyond the 5000km value. Have there been tests done with longer localization lengths ?*

This is an important question that we need to address. We have now completed tests beyond 5000 km. The height-only assimilation does optimize at 5000 km (with and without NNMI) for the EnKF- $uv$ , but for the EnKF- $\psi\chi$  height-only assimilation optimizes at 7000 km (with and without NNMI). This results in slightly smaller analysis errors and slightly higher WEP than currently reported. For example, below we show the WEP out to 8000 km (compare with original Figure 9f). We will modify the paper to account for these new results.



1 2 3 4 5 6 7 8  
Length [x 1000 km]

We revised Figure 9 to extend all error metrics out to 8000 km. We also changed the optimal results for the EnKF- $\psi\chi$  height-only case in Table 1 and in Figure 10. Minor modifications to the text were included to account for the new results.

*Also, considering that ozone assimilation and height assimilation products behave differently when varying localization lengths, why has a single localization length parameter strategy been retained for the combined ozone and height assimilation experiment ?*

This single localization strategy was used as a simple method for maintaining a consistent localization approach among all experiments in this first study on tracer-wind extraction using the EnKF. It would be interesting to study the application different spatial localization functions for different model variables and the resulting effects on multivariate correlations. However, this is beyond the scope of the present work.

We now include a brief statement on this subject in Section 3.3.

### **Response to Referee 2 (Alan Geer)**

*1) P3958, L22 "...the background error covariance does not include tracer-wind correlations... This limitation can be overcome by using an ensemble Kalman filter...". Note that limitations of 4D-Var can also be addressed using hybrid methods and this is increasingly popular at operational centres (e.g. 4D-Var background errors can be generated using an ensemble method). More generally, though this should definitely not become a "4D-Var versus EnKF" paper, it would be nice if the authors could briefly compare back to their experiences when they performed a very similar study using 4D-Var (perhaps a short discussion or a few sentences in the conclusion?).*

We are actually developing hybrid methods using the shallow water model as a follow-up to this paper. For the hybrid we will blend the static covariance from 4D-Var with the flow-dependent covariance from the EnKF. We will mention hybrid models as an additional option in the Introduction. We will also include some comments in the conclusion related to our 4D-Var experience. A direct comparison is not possible, since the observations in the 4D-Var paper differed in two major aspects: (1) only tracer data were assimilated, and (2) the observation grid was much different from that used in the EnKF.

We added a comment on the hybrid approach in the Introduction and included a brief discussion of 4D-Var vs. EnKF in the Conclusions section. Preliminary results show that the hybrid 4D-Var coupled to the EnKF works very well in this context.

**2) P3961, L10 Why is the observation error covariance matrix referred to as "R\_ens"? This implies, to me at least, there might be something special about how it is created. Would not "R" be sufficient?**

R would be sufficient here since we use a diagonal matrix based on the specified standard deviations rather than a statistical covariance matrix calculated from the randomly perturbed observations. In principle these should be the same, but in practice, with limited ensemble size the statistical covariance is not exactly diagonal. We will change the notation to "R".

R\_ens is changed to R throughout the paper.

**3) P3962 L4, "To avoid filter divergence we apply an inflation factor to maintain reasonable spread in the ensemble". The text needs to say both what the inflation factor is applied to and how it is done.**

The inflation factor is a scalar value multiplied by each state vector element in the ensemble perturbations in order to alter the globally-averaged SPREAD (calculated using one or more of the state variables) so that it matches the globally-averaged RMSE. For the EnKF- $uv$  system we alter the SPREAD in the vector wind error (V\_SPREAD in Eq. 6) so that it matches the vector wind RMSE (V\_RMSE in Eq. 5). For the EnKF- $\psi\chi$  system we alter the SPREAD in the streamfunction so that it matches the streamfunction RMSE. Although the inflation factor is calculated using a subset of state variables, it is applied to all variables (including height and ozone for EnKF- $uv$  and including height, ozone, and velocity potential for EnKF- $\psi\chi$ ). We will make this more explicit in the text.

Additional text is added to clarify how the inflation is applied. In addition, Eqs (5) and (6) are altered to explicitly show how the calculations are done with vector wind error for EnKF- $uv$  and streamfunction for EnKF- $\psi\chi$ .

**4) Equations 8 and 9 seem slightly confusing to me. Why is only the latitude dependence made explicit? How was a latitude/longitude/time varying error reduced to a latitude/time varying RMSE? I think I can guess, but please add a bit more explanation. Note also that later, in equation 11 and associated discussions, you are giving a lot more detail about what are probably very similar calculations, but this time explicitly showing how the latitude-dependent RMSE has been computed.**

The latitude dependence is made explicit since we show errors as a function of latitude in Figure 10. Eq. (11) does show how the RMS is calculated separately for each latitude. This should be explained as part of the discussion in Equations (8) and (9). Similarly, the area-weighting given in Eq. (12) is the explicit formulation of what is said in words at the bottom of p. 3969. We will edit the text to make this more explicit.

We now explain why the latitude dependence is explicit and also include the RMSE equation to help explain Equation (8). In addition, we include the area-weighting explicitly in the WEP calculation.

**5) P3972, L16-23. Discussion around the chi-squared metric seems to start with a nonnormalised version (which is expected to be equal to the number of observations) and moves to a normalised version (expected to equal 1) without explaining properly how the second is obtained, and without changing terminology to distinguish the two. So it comes as a shock in the last sentence when a "chi-squared" of around 1 is considered good.**

Thank you for pointing this out. It is indeed the normalized “chi-squared” that should equal 1. We will fix the text to make this clear.

We now define chi-squared as the normalized version so that the expected value is unambiguously 1.

**6) p3976, l22: "It appears that combining height observations and ozone observations acts as a filter to dampen the GW that would otherwise be generated by the ozone observations alone". I am not sure the "filter" idea is necessary, and it would be good to explain what it means physically. Instead, is it possible that you simply require both height and ozone observations to properly constrain a shallow water model? Height observations just constrain height and the balanced part of the wind, but leave the unbalanced part of the wind unconstrained. That could allow GWs to develop. But the ozone observations could help constrain the unbalanced part of the wind field, stopping spurious GWs developing.**

We will omit the “filter” concept from our discussion. Our results show that if we only assimilate ozone observations there is a lot of imbalance (Figure 9d), while height only assimilation produces much less imbalance (Figure 9i). Combined height and ozone assimilation produces an intermediate amount of imbalance. This suggests that adding height observations to the ozone system reduces the imbalance (excites fewer gravity waves) compared to ozone alone (Figure 9n vs. 9d). Similarly, adding ozone observations to the height system increases the imbalance (Figure 9n vs. 9i). We aren’t sure exactly how this process works, but we suspect that the cross-covariances of ozone/wind and ozone/height are not as balanced as the cross-covariance of height/wind. Your discussion of height/ozone constraining different parts of the wind is interesting. In our truth run there is almost no imbalance, so any imbalances is “unwanted”. But if the truth run had significant imbalance that we needed to analyze, it may be that ozone observations would be more useful for the unbalanced part of the wind, while height would be more useful for constraining the balanced part of the wind.

We removed the filter concept from the discussion to avoid any unnecessary confusion.

# Wind extraction potential from ensemble Kalman filter assimilation of stratospheric ozone using a global shallow water model

1

2 **D. R. Allen<sup>1</sup>, K. W. Hoppel<sup>1</sup> and D. D. Kuhl<sup>1</sup>**

3 [1]{Remote Sensing Division, Naval Research Laboratory, Washington, DC, USA}

4 Correspondence to D. R. Allen (douglas.allen@nrl.navy.mil)

## 5 **Abstract**

6

7 The feasibility of extracting wind information from stratospheric ozone observations is tested  
8 using ensemble Kalman filter (EnKF) data assimilation (DA) and a global shallow water model  
9 that includes advection of an ozone-like tracer. Simulated observations are created from a truth  
10 run (TR) that resembles the Northern Hemisphere winter stratosphere with a polar vortex  
11 disturbed by planetary-scale wave forcing. Ozone observations mimic sampling of a polar-  
12 orbiting satellite, while geopotential height observations are randomly placed in space and time.  
13 10-day EnKF experiments are performed assimilating ozone, height, or both. The DA is also  
14 implemented using two different pairs of flow variables: zonal and meridional wind (EnKF- $uv$ )  
15 and streamfunction and velocity potential (EnKF- $\psi\chi$ ). Each experiment is tuned for optimal  
16 localization length, while the ensemble spread is adaptively inflated using the TR. The  
17 experiments are evaluated using the maximum wind extraction potential (WEP). Ozone-only  
18 assimilation improves winds (WEP = 46% for EnKF- $uv$ , and 58% for EnKF- $\psi\chi$ ), but suffers  
19 from spurious gravity wave generation. Application of nonlinear normal mode initialization  
20 (NMI) greatly reduces the unwanted imbalance and increases the WEP for EnKF- $uv$  (84%) and  
21 EnKF- $\psi\chi$  (81%). Assimilation of only height observations also improved the winds (WEP =  
22 | ~~5960~~% for EnKF- $uv$ , and ~~6769~~% for EnKF- $\psi\chi$ ), with much less imbalance compared to the  
23 ozone experiment. The assimilation of both height and ozone performed the best, with WEP  
24 increasing to ~87% (~90% with NMI) for both EnKF- $uv$  and EnKF- $\psi\chi$ , demonstrating that  
25 wind extraction from ozone assimilation can be beneficial even in a data-rich environment.

1 Ozone assimilation particularly improves the tropical winds, which are not well constrained by  
2 height observations due to lack of geostrophy.

### 3 **1. Introduction**

4 A key missing component of the global observing system (GOS) is measurement of the three-  
5 dimensional global wind (World Meteorological Organization, 2000). Upper air wind  
6 observations from radiosondes, pilot reports, and cloud and water vapor feature-tracking leave  
7 large gaps, particularly in the tropics, Southern Ocean, and in most of the stratosphere and  
8 mesosphere. Spaceborne Doppler Wind Lidar (DWL) has been proposed as the potential  
9 “missing link” in the GOS (Baker, 2014). When placed in low earth orbit, DWL can provide  
10 daily global wind profiles throughout the troposphere and lower stratosphere (National Research  
11 Council, 2007). The Atmospheric Dynamics Mission (ADM-Aeolus) (Stoffelen et al., 2005), will  
12 provide a proof-of-concept of this capability. However, the measurements will be limited to a  
13 single line-of-sight wind component, altitudes below ~26 km, and simple along-track (as  
14 opposed to sweeping or conical) sampling. While future spaceborne DWL missions may provide  
15 improved observing capabilities, the technical challenges make this a very difficult and  
16 expensive solution to the problem of inadequate wind observations.

17 Another potential source of dynamical information comes from assimilation of trace gas (tracer)  
18 observations in a 4D data assimilation system (DAS) that dynamically couples tracer and wind.  
19 The investigation of algorithms to extract wind information from tracers started with 1D and 2D  
20 simulations by Daley (1995, 1996) and Riishøjgaard (1996). These studies showed that wind  
21 information could be extracted from tracer observations when the continuity equation was  
22 coupled to the dynamical equations via either a 4D-Var algorithm or an extended Kalman filter  
23 (EKF). Extensions to the full 3D atmosphere were performed in 4D-Var experiments by Peuch et  
24 al. (2000), Semane et al. (2009), and Allen et al. (2013). These further supported the potential of  
25 tracer assimilation to benefit the winds, but also highlighted limitations due to paucity of  
26 observations, insufficient data quality, and inadequate modeling of tracers in the forecast model,  
27 as well as phenomenological limitations due to geophysical variability.

28 Assimilation of infrared and microwave humidity channels from geostationary and polar-orbiting  
29 satellites has been shown to benefit tropospheric analyses and forecasts in the European Centre

1 for Medium-Range Weather Forecasts (ECMWF) 4D-Var system (Andersson et al., 2007;  
2 Peubey and McNally, 2009). Peubey and McNally (2009) isolated the mechanisms whereby  
3 geostationary clear-sky radiances can impact the wind analyses in 4D-Var and showed that the  
4 dominant factor involves adjustment of the wind field in order to match observed humidity  
5 features (the so-called “tracer advection effect”). However, attempts to assimilate stratospheric  
6 ozone using 4D-Var algorithms and the resultant dynamical coupling have previously resulted in  
7 problems in operational numerical weather prediction (NWP) (Han and McNally, 2010; Dragani  
8 and McNally, 2013). These assimilation challenges led Allen et al. (2014) to re-examine the  
9 stratospheric tracer-wind problem at a more fundamental level using 4D-Var assimilation studies  
10 with a shallow water model (SWM) coupled to the tracer continuity equation. This idealized  
11 system allowed Allen et al. (2014) to probe the limits of wind extraction from assimilation of  
12 three readily-measured long-lived tracers: ozone (O<sub>3</sub>), nitrous oxide (N<sub>2</sub>O), and water vapor. It  
13 was shown that assimilation of global hourly tracer data was sufficient to analyze the horizontal  
14 wind components to a high degree of accuracy ( $\sim 0.3 \text{ m s}^{-1}$  random error for O<sub>3</sub> and N<sub>2</sub>O).

15 While 4D-Var couples tracers and dynamical variables through the tangent linear model and its  
16 adjoint, the initial background error covariance normally does not include tracer-wind  
17 correlations (these correlations develop implicitly over the assimilation window). This limitation  
18 may be overcome by using an ensemble Kalman filter (EnKF) in which the error covariance  
19 between tracer and wind ~~are~~is explicitly calculated by the ensemble statistics. Milewski and  
20 Bourqui (2011) assimilated ozone and temperature profiles in an EnKF system using a 3D model  
21 at relatively low resolution (spectral triangular truncation T21). They showed that background  
22 error covariances are able to propagate information from the observed variables to wind. In  
23 particular, assimilation of either ozone or temperature observations in a polar-orbiting sampling  
24 pattern significantly improved the wind analysis. Another approach to enhancing the tracer-wind  
25 interaction within 4D-Var is to blend the static covariance with a flow-dependent ensemble  
26 covariance. This hybrid 4D-Var method is becoming increasingly popular at operational NWP  
27 centers. We are developing a hybrid system within the SWM framework to study tracer-wind  
28 interaction, which we plan to present in a follow-up paper.

29 In this paper, we take a similar approach to Milewski and Bourqui (2011), except that we use the  
30 SWM forecast model (at T42 resolution), and we assimilate ozone and height (in lieu of

1 temperature for the SWM) observations, both separately and together, in order to examine  
2 whether value is added by assimilating ozone observations into a system already constrained by  
3 other observations. The SWM has been used in both 4D-Var (Courtier and Talagrand, 1990;  
4 Polavarapu et al., 2000; Jung et al., 2014) and EnKF (Kepert, 2009, 2011) simulations, since it  
5 provides a sufficiently complex system to simulate the key physical relations of the horizontal  
6 flow, including both slow balanced and fast unbalanced modes. As explained by Kepert (2009),  
7 the SWM provides a severe test for assimilation, since the weak dissipation will not remove  
8 imbalances introduced in the analysis; they will rather accumulate with time.

9 One of the goals of the current study is to probe the limits of ozone-wind extraction in an EnKF  
10 system. To accomplish this, it is necessary to quantify (and remove, if possible) spurious  
11 imbalance generated from noisy observations and imperfect modeling of background error  
12 covariances. A wide range of studies has been performed to examine balance in the context of  
13 4D data assimilation. For example, Neef et al. (2006, 2009) investigated balance with a low-  
14 order Lorenz-type model with the EKF and EnKF. Imbalance within SWM-DAS systems was  
15 analyzed in both 4D-Var (Courtier and Talagrand, 1990; Polavarapu et al., 2000) and EnKF  
16 (Kepert, 2009, 2011) using digital filter and nonlinear normal mode initialization techniques.  
17 Mitchell and Houtekamer (2002) considered the influence of covariance localization on balance  
18 with a 3D dry, global, primitive-equation model. In all of these studies, imbalance was shown to  
19 be a serious issue in 4D DAS. None of these studies was designed to examine balance in the  
20 context of the tracer assimilation problem, however. As part of this study we attempt to isolate  
21 and to the extent possible remove imbalance in order to minimize the analysis errors and to  
22 determine the extent to which the wind can be constrained by ozone observations.

23 The layout of the paper is as follows. Section 2 describes the SWM-DAS, including the forecast  
24 model, the EnKF, and the normal mode initialization procedure. Section 3 describes the  
25 experimental design and the error diagnostics. Section 4 presents the results and discussion from  
26 the three assimilation experiments, and conclusions are provided in Section 5.



## 1 **2. Model description**

### 2 2.1 Forecast model

3 The forecast model is a spectral SWM based on the vorticity-divergence formulation in Section  
4 2a of Ritchie et al. (1988), with the inclusion of fourth-order semi-implicit diffusion applied to  
5 the vorticity, divergence, and geopotential. A spectral advection equation is coupled to the  
6 SWM, solving for the mixing ratio of a passive tracer as a function of time using the same  
7 fourth-order diffusion operator. We call the combined four equation system the Shallow Water  
8 Model with Tracer (SWM<sup>T</sup>). The system is run at triangular truncation T42, with model fields  
9 saved on the Gaussian grid (128 longitudes  $\times$  64 latitudes, for a grid resolution of  $\sim 2.8^\circ$  at the  
10 equator). The discretization uses a leap-frog time integration and a semi-implicit approximation  
11 for terms that produce gravity waves (Ritchie, 1988). To restart the model after assimilating data,  
12 an Euler forward time stepping method is applied. The global mean geopotential height  $H$  is  
13 specified to be 10 km, resulting in a gravity wave speed ( $\sqrt{gH}$ , where  $g$  is the earth's  
14 gravitational acceleration) of  $313 \text{ m s}^{-1}$ . To avoid numerical instability due to gravity waves, a  
15 short model time step of 120 s is used for all SWM<sup>T</sup> forecasts. The diffusion coefficient is set to  
16  $5.0 \times 10^{15} \text{ m}^4 \text{ s}^{-1}$ , which provides an e-folding damping for the highest wavenumber of  
17 approximately one day.

### 18 2.2 Ensemble Kalman filter

19 To assimilate data into the SWM<sup>T</sup> system, we use the “perturbed observations” EnKF  
20 (Houtekamer and Mitchell, 1998; Evenson, 2003). The system solves for  $N_{ens}$  analysis states  
21 using the Kalman filter equation for the state vector  $\mathbf{x}$  of size  $N_{state}$ .

$$\mathbf{x}_i^a = \mathbf{x}_i^b + \mathbf{K}_{ens} \mathbf{d}_i \quad (1)$$

22 where  $a$  and  $b$  superscripts indicate analysis and background, and  $i = 1 \dots N_{ens}$  is an index for  
23 ensemble member.  $\mathbf{d}_i = \mathbf{y}_i - \mathbf{H}\mathbf{x}_i^b$  is the vector of innovations for member  $i$ ,  $\mathbf{y}_i$  is the vector of  
24 perturbed observations, and  $\mathbf{H}$  is the (linear) observation operator. The ensemble-based Kalman  
25 gain matrix is defined as follows

$$\mathbf{K}_{ens} = \mathbf{P}_{ens}^b \mathbf{H}^T [\mathbf{H}\mathbf{P}_{ens}^b \mathbf{H}^T + \mathbf{R}]^{-1} \quad (2)$$

1 with the ensemble background error covariance calculated by

$$\mathbf{P}_{ens}^b = \frac{1}{N_{ens} - 1} \sum_{i=1}^{N_{ens}} (\mathbf{x}_i^b - \overline{\mathbf{x}}^b) (\mathbf{x}_i^b - \overline{\mathbf{x}}^b)^T. \quad (3)$$

2 Here the overbar indicates the ensemble mean and  $\mathbf{R}$  is the ~~ensemble~~ observation error  
3 covariance matrix. The background state is calculated using the non-linear SWM<sup>T</sup> forecast model  
4  $M$ , subject to initial conditions

$$\mathbf{x}_i^b(t_n) = M[\mathbf{x}_i^b(t_{n-1})] \quad (4)$$

5 where  $n$  is an ~~an~~ time-index for ~~analysis-model~~ times ( $t_n$ ). Note that the SWM<sup>T</sup> time step (120 s) is  
6 less than the analysis time step (20 min), such that there are 10 time steps (10 applications of Eq.  
7 4) between analyses. so one application of Eq. 4 represents multiple SWM<sup>T</sup> time steps. At each  
8 analysis time, all the observations within the analysis time bin are assimilated simultaneously as  
9 a single batch.

10

11 The EnKF analysis equation can be solved using different combinations of state variables. In this  
12 study, we compare results using zonal wind, meridional wind, height, and ozone  $\mathbf{x} = [u, v, z, q]$   
13 (the EnKF- $uv$  system) and streamfunction, velocity potential, height, and ozone  $\mathbf{x} = [\psi, \chi, z, q]$   
14 (the EnKF- $\psi\chi$  system). The latter combination was shown by Kepert (2009) to result in better  
15 balance of increments in a SWM-EnKF system with Schur product localization (discussed  
16 further below). We will test this for the SWM<sup>T</sup> system with ozone and height observations.

17

18 To avoid filter divergence, we apply an inflation factor to maintain reasonable spread in the  
19 ensemble. The scalar inflation factor is multiplied by the background ensemble perturbations,  
20  $\mathbf{x}_i^b - \overline{\mathbf{x}}^b$ , in order to control the global average SPREAD. The SPREAD is forced to match the  
21 global Root Mean Square Error (RMSE) of either the vector wind (for EnKF- $uv$ ) or the  
22 streamfunction (for EnKF- $\psi\chi$ ). ~~For EnKF- $uv$ , the factor is tuned so that the background global~~  
23 ~~Root Mean Square Error (RMSE) of the ensemble mean vector wind matches the ensemble~~  
24 ~~SPREAD.~~ The RMSE and SPREAD for vector wind are defined as

1

$$V_{RMSE} = \sqrt{\frac{1}{N_{state}} \sum_{j=1}^{N_{state}} [\bar{u}_j^b - u_j^{TR}]^2 + [\bar{v}_j^b - v_j^{TR}]^2} \quad (5)$$

$$V_{SPREAD} = \sqrt{\frac{1}{(N_{ens} - 1)N_{state}} \sum_{i=1}^{N_{ens}} \sum_{j=1}^{N_{state}} [u_{i,j}^b - \bar{u}_j]^2 + [v_{i,j}^b - \bar{v}_j]^2}$$

$$V_{SPREAD} = \sqrt{\frac{1}{(N_{ens} - 1)N_{state}} \sum_{i=1}^{N_{ens}} \sum_{j=1}^{N_{state}} [u_{i,j}^b - \bar{u}_j]^2 + [v_{i,j}^b - \bar{v}_j]^2} \quad (6)$$

2 where  $V$  represents the magnitude of the vector wind ( $\mathbf{V}$ ) and TR indicates the truth run  
 3 (described in Section 3.1). ~~For EnKF- $\psi$ , the streamfunction is used rather than the vector wind~~  
 4 ~~in the covariance tuning.~~ For streamfunction ( $\psi$ ) the RMSE and SPREAD are defined as

5

$$\psi_{RMSE} = \sqrt{\frac{1}{N_{state}} \sum_{j=1}^{N_{state}} [\bar{\psi}_j^b - \psi_j^{TR}]^2}$$

(6)

$$\psi_{SPREAD} = \sqrt{\frac{1}{(N_{ens} - 1)N_{state}} \sum_{i=1}^{N_{ens}} \sum_{j=1}^{N_{state}} [\psi_{i,j}^b - \bar{\psi}_j]^2}$$

6 The inflation factor is calculated as either  $\xi = V_{RMSE} / V_{SPREAD}$  or  $\xi = \psi_{RMSE} / \psi_{SPREAD}$ . While the  
 7 inflation factor is calculated using only the wind or streamfunction, it is applied to the entire state  
 8 vector for each ensemble member via  $\xi(\mathbf{x}_i^b - \bar{\mathbf{x}}^b)$ . ~~In both cases, T~~the calculations of RMSE and

9 SPREAD are not area-weighted, and therefore may be somewhat biased to match the higher  
 10 latitudes, since the Gaussian grid is used. This tuning takes a similar approach to the 4D-Var  
 11 simulations of Allen et al. (2014) in which the background error variances were modified to  
 12 match the global RMSE of the tracer and wind components. This adaptive tuning approach  
 13 provides a flexible way to examine how the system behaves over a wide range of parameters,  
 14 without needing to separately tune the inflation factor for each case. It is of course not practical

1 in an operational setting, since the true state is unknown, but for this idealized study it works  
 2 well to prevent filter divergence.

3  
 4 To avoid spurious long-range correlations, localization is applied to the background error  
 5 covariance. We apply the elementwise (Schur product) approach (e.g., Houtekamer and Mitchell,  
 6 2001) using Eq. (4.10) of Gaspari and Cohn (1999). The localization matrix  $\mathbf{S}$  is applied directly  
 7 to the background error covariance so the gain matrix becomes

$$\mathbf{K}_{ens} = \mathbf{S} \circ \mathbf{P}_{ens}^b \mathbf{H}^T [\mathbf{H} \mathbf{S} \circ \mathbf{P}_{ens}^b \mathbf{H}^T + \mathbf{R}]^{-1}. \quad (7)$$

8 To illustrate the ozone-wind interaction in the SWM<sup>T</sup>-EnKF system, Fig. 1 shows the ensemble  
 9 mean analysis increments  $\mathbf{K}_{ens} \bar{\mathbf{d}}$  for assimilation of a single ozone observation at 120°E  
 10 longitude, 40°N latitude for the EnKF- $uv$  and EnKF- $\psi\chi$  systems. For the EnKF- $\psi\chi$ , we convert  
 11 the increments to wind increments after the analysis step. Specification of the initial 100-member  
 12 ensemble for this system will be discussed in Section 3. The positive ensemble mean ozone  
 13 innovation ( $\bar{\mathbf{d}}=0.21$  parts per million by volume, ppmv) results in a positive ozone increment in  
 14 the vicinity of the observation with maximum of 0.11 ppmv. Since the height correlates  
 15 positively with ozone, a positive height increment also occurs (maximum of 84 m). Note that the  
 16 ozone and height increments are similar for both systems, since these variables are unchanged;  
 17 slight differences are due to differences in tuning of the background error covariances. The wind  
 18 increments are very different, however. While both show anticyclonic circulation around the  
 19 positive height increment, the winds are much stronger in the EnKF- $\psi\chi$ . As explained by Kepert  
 20 (2009, 2011) the weakening of the winds in the EnKF- $uv$  is due the effects of localization, which  
 21 acts to decrease the local balance. As shown below, this adversely affects the system by  
 22 generating spurious gravity waves.

### 23 2.3 Normal mode initialization

24 In general, analysis increments may project onto both slow balanced modes and fast unbalanced  
 25 modes. Unless there is sufficient information in the background error covariance to distribute  
 26 increments in a balanced way, the unbalanced modes will enter the system, and it may be  
 27 difficult to remove these modes with limited observations (Neef et al., 2006, 2009). To quantify  
 28 the imbalance in the SWM-EnKF, we use a nonlinear normal mode initialization (NMI)

1 procedure (Machenhauer, 1977), which has in the past been extensively used in NWP to reduce  
2 the impact of inertia gravity waves caused by imbalance in the analysis increments. While digital  
3 filter initialization (e.g., Fillion et al., 1995) is more commonly used in NWP today, NMI allows  
4 discrimination between the gravity wave and rotational wave modes, which is very useful in the  
5 SWM context. Kepert (2009) used NMI to analyze imbalance caused by localization in the  
6 SWM-EnKF framework, and showed that while gravity waves can be reduced by judicious  
7 choice of balance constraints, some initialization may still be necessary in the EnKF (see also the  
8 discussion in Lorenc, 2003).

9  
10 For example, the single-observation increments in Fig. 1 result in unbalanced motions in both  
11 versions of the SWM<sup>T</sup> system. Figure 2 shows the divergence anomalies due to the single-  
12 observation increments. These anomalies propagate radially outward from the observation  
13 location, as seen in these maps at 2-h intervals. Maps at later times (not shown) indicate that  
14 these oscillations propagate around the globe in ~1.5 days, consistent with waves traveling at the  
15 gravity wave phase speed of this system. The EnKF- $\psi\chi$  increments result in smaller divergence  
16 fields than the EnKF- $uv$ ; the maximum divergence anomaly at 1200 s for the EnKF- $\psi\chi$  is ~13%  
17 of that caused by the EnKF- $uv$ , consistent with less imbalance. However, initialization may still  
18 be necessary in both systems to remove this spurious gravity “noise.”

19  
20 In order to “initialize” the system (i.e., apply NMI to the analysis state vector), we first need the  
21 normal modes (NM) of the SWM system. These were calculated using the formulation outlined  
22 in Hogan et al. (1992). The resulting NM frequencies are shown in Fig. 3 as a function of zonal  
23 wavenumber and mode type. Negative (positive) wavenumbers indicate westward (eastward)  
24 propagating modes. These modes are separated into westward and eastward gravity wave (GW)  
25 and westward rotational wave (RW) modes. To balance the GW modes, we apply the  
26 Machenhauer (1977) condition, which reduces the time tendencies of the complex amplitudes of  
27 the modes. We apply five iterations to solve the nonlinear balance equation using a single 120 s  
28 time step for the calculation of the tendencies. We choose a linear cutoff frequency of 1.0 day<sup>-1</sup>,  
29 which attempts to balance all traveling modes except for one eastward wave 1 GW mode (see  
30 Fig. 3a).

31

1 In this study, we apply NMI to the ensemble mean analyzed fields as a post-processing  
2 diagnostic to quantify the degree of imbalance. The goal is to tune the EnKF system to minimize  
3 unwanted imbalance, without having to rely on applying NMI within the DAS. One reason to  
4 avoid initialization in the EnKF cycling is that it fails to distinguish real and spurious gravity  
5 waves, and can therefore potentially move the system away from the truth. Another reason is that  
6 running NMI in the EnKF would involve initializing each ensemble member separately, since  
7 different modes may be excited in each member due to the perturbed observations, which adds  
8 significantly to the computational expense. In principle, if the unbalanced modes do not interact  
9 much with the balanced components of the flow, then it should not matter whether the balancing  
10 is done before or after the assimilation. Williamson and Temperton (1981) showed that forecasts  
11 made with initialized data produced virtually identical results to forecasts with uninitialized data  
12 followed by initialization. This suggests that the high-frequency GW do not interact much with  
13 the low-frequency RW, but rather can be largely considered “noise” in the system that can, in  
14 principle, be filtered out. To test whether this is true for the system run here, we compared results  
15 using NMI cycling and NMI post-processing for the optimal runs of the three experiments  
16 examined in Section 4. Differences in wind extraction potential (defined in Section 3) were  $\sim 1\%$   
17 or less for all runs, except for height only assimilation with the EnKF-*uv* system, which showed  
18 an improvement of 5% for NMI cycling over NMI post-processing. Assimilation of height  
19 observations is likely more sensitive to GW noise, which impacts the height directly, while the  
20 tracer is only indirectly impacted via the divergent component of the wind, which is small  
21 compared to the rotational wind.

22

23 To illustrate the influence of NMI post-processing, Fig. 4 shows the true divergence along with  
24 the analyzed divergence with and without NMI for a sample field two days into an ozone  
25 assimilation run. Whereas the true divergence is rather smooth, the uninitialized divergence  
26 shows considerable noise. After applying NMI, the analyzed divergence looks much more like  
27 the truth, indicating that the noise was due largely to spurious unbalanced modes. We note that  
28 this rather dramatic improvement from application of NMI is partly illustrating sensitivities in  
29 the SWM. Whereas in a full NWP system, physical and radiative processes may dampen the  
30 gravity waves, in the SWM with weak diffusion, the waves can remain in the system for a long

1 time, unless assimilated data are at sufficient sampling frequency and precision to resolve the  
2 waves.

### 3 **3. Experimental design**

#### 4 **3.1 Truth run**

5 The truth run (TR) is designed to simulate Northern Hemisphere (NH) winter conditions in the  
6 middle stratosphere (the same TR was used in the 4D-Var tracer assimilation study by Allen et  
7 al., 2014). The initial conditions for [the](#) SWM<sup>T</sup> include zero meridional wind and a zonally-  
8 symmetric zonal wind that varies with latitude ( $\varphi$ ) as  $u(\varphi) = u_{\max} \sin(2\varphi)$  in the NH and is zero  
9 in the Southern Hemisphere (SH), with  $u_{\max} = 60 \text{ m s}^{-1}$ . The geopotential height is specified  
10 using the gradient wind balance with a global mean height of 10 km. The initial ozone is  
11 calculated using Aura Microwave Limb Sounder (MLS) ozone data (Waters et al., 1999; Livesey  
12 et al., 2011). The data are selected for a period with weak planetary wave activity (1-15 March  
13 2011) and are interpolated to the 850 K isentropic level (approximately 32 km altitude or 10  
14 hPa), representative of middle stratosphere conditions. The zonal mean and time mean mixing  
15 ratio as a function of latitude was calculated for this period and interpolated to the Gaussian grid.  
16 The ozone is treated as passive (i.e., no chemical source/sink) and there is no radiative  
17 interaction between ozone and dynamics. Note that in the TR there are no “restarts.” Therefore,  
18 an assimilation cycling run, which restarts after each cycle with a forward Euler step, would  
19 produce a slightly different result from the continuous TR, even if no data were assimilated. We  
20 could, in principle, restart the TR at the regular analysis time intervals, as was done in Kepert  
21 (2009); however, test runs performed with and without restarts in the TR resulted in negligible  
22 differences.

23  
24 In order to create a realistic scenario of the NH winter stratosphere, the TR is forced by the  
25 bottom topography being raised and lowered in order to simulate planetary-scale waves (as in  
26 Norton, 1994). A mountain of height 1250 m is created with a 20 day cycle (4 days ramping up,  
27 12 days constant, and 4 days ramping down). The mountain is a zonal wave 1 feature that peaks  
28 at 45°N. The topography is turned off after 20 days. Since the assimilation period corresponds to  
29 days 20-30 of this TR, there is no surface topography during the assimilation. NH maps of the

1 ozone and height fields for the TR are provided in Fig. 5a-f. On day 20, a strong anticyclone  
2 (indicated by “H”) is present near 180° longitude, resembling an “Aleutian High,” with elevated  
3 ozone values. The polar vortex (indicated by “L”), identified by low ozone, is displaced off the  
4 pole into a comma shape. Over the next 10 days, the “Aleutian High” diminishes in strength and  
5 the vortex moves over the pole. Strong ozone advection occurs throughout this period. For  
6 example, a long tongue of lower ozone mixing ratio forms around a secondary anticyclone  
7 centered near 60°E longitude on day 28. This dynamical scenario produced by topographic wave  
8 forcing in the SMW<sup>T</sup> provides a realistic representation of the final stages of a stratospheric  
9 minor warming. In the SH (Fig. 5g-l), a strong anticyclone is centered just off the pole on Day  
10 20. This anticyclone (“H”) propagates westward around the pole, making one cycle over this 10  
11 d period. A weaker cyclone (“L”) also propagates westward around the pole opposite to the  
12 anticyclone. The ozone is advected along with these features, with relatively high (low) ozone in  
13 the anticyclone (cyclone). The westward flow in the SH is consistent with the easterly summer  
14 flow in the middle stratosphere (Andrews et al., 1987). Additional maps of potential vorticity and  
15 ozone for this TR are provided in Fig. 2 of Allen et al. (2014).

## 16 3.2 Observations

17 Observations are simulated by sampling the TR ozone and height fields using a bi-linear  
18 interpolation in latitude and longitude. Gaussian random error is then added with a specified  
19 standard deviation. The error standard deviation for ozone was set at 0.08 ppmv, which is 1% of  
20 the initial global mean, while the height error standard deviation was set to 50 m. The height  
21 error can be approximately related to stratospheric temperature error by using a climatological  
22 estimate of the equator-to-pole gradient of temperature with respect to height of ~5 K/km. Using  
23 this conversion factor, 50 m error corresponds to ~0.25 K. Both the ozone and height errors are  
24 smaller than those of any current operational instrument. The goal here is not to evaluate an  
25 actual observing system, but to demonstrate ozone-wind extraction in an idealized system. The  
26 observation errors are assumed to be uncorrelated, so the observation error covariance **R** is  
27 diagonal with elements given by the square of the error standard deviations.

28

29 Two sampling methods are performed (see Fig. 6). For ozone, the observation locations are taken  
30 from real ozone observations from the Aura MLS polar-orbiting satellite (sampling frequency of



1 ~3450 observations per day). For height, pseudo-random sampling in space and time is  
2 performed in order to approximate the global coverage provided by microwave and infrared  
3 radiance sensors. For each successive height observation, the sampling occurs at one of 3840  
4 latitude/longitude points on an icosahedral equal-area grid. This allows the observations to not be  
5 too clumped together and provides a way to scale upward to a global equal area grid sampling, as  
6 was used in Allen et al. (2013). We choose the average data frequency for the height  
7 observations to be the same as the MLS sampling frequency (~3450 per day). In time, the height  
8 observations occur randomly over 10 days. For both observation types, the observation time is  
9 assigned to the nearest 20-min interval (0, 20, or 40 min). Since the analysis is performed  
10 sequentially every 20 minutes, time-interpolation is not necessary for observations.

### 11 3.3 Assimilation experiments

12  
13 We use 100 ensemble members for all experiments in this paper. The initial ensemble  
14 perturbations are generated by sampling the TR fields at 6-h intervals (starting day 21) and then  
15 removing the ensemble mean. The assimilation experiments begin 20 days into the TR, with the  
16 ensemble perturbations centered on TR fields that are offset 6 h from the initial time. This initial  
17 6 h offset, or mismatch, between the TR and the background fields is the source of the initial  
18 background error. In Section 4 we present results from three different experiments: (1) ozone  
19 only, (2) height only, and (3) ozone and height. For each experiment, assimilation runs were  
20 done for both EnKF- $uv$  and EnKF- $\psi\chi$  using localization lengths from 1000 to ~~5000~~ 8000 km, in  
21 500 km increments (note that ozone only experiments failed to converge at the maximum  
22 localization length of 8000 km). Tuning the length separately for each experiment and EnKF is  
23 necessary, since the DA responds differently depending on the field(s) observed and the analysis  
24 variables used. For each experiment we use the same localization length for all state variables.  
25 Further optimization may occur by applying different localization functions to different  
26 variables, but this is beyond the scope of this first study on tracer-wind interaction using the  
27 EnKF. Since inflation is automatically adjusted in a self-consistent manner with the TR, it does  
28 not require tuning. Post-processing with NMI was also performed for each run. We note here that  
29 the same forecast model is used for the TR and for the assimilation experiments (i.e., “identical  
30 twin” experiments), making results overly optimistic.

### 1 3.4 Error metrics

2 To diagnose the results, several error metrics are examined, including the global RMSE (area-  
 3 weighted) of the  $u$ ,  $v$ ,  $z$ , and  $q$ , along with the Wind Extraction Potential (WEP). Allen et al.  
 4 (2014) defined WEP as a normalized diagnostic of the impact of tracer assimilation on the  
 5 dynamics. The WEP is determined by first calculating the analyzed RMSE of the vector wind as  
 6 a function of latitude ( $\varphi$ ) and time ( $t$ ):

$$V_{RMSE}(\varphi, t) = \sqrt{[u_{RMSE}(\varphi, t)]^2 + [v_{RMSE}(\varphi, t)]^2} \quad (8)$$

7 where  $u_{RMSE}(\varphi, t) = \sqrt{\sum_{\lambda} [u(\lambda, \varphi, t) - u^{TR}(\lambda, \varphi, t)]^2 / N_{LON}}$  is the RMSE calculated around a  
 8 latitude circle containing  $N_{LON}$  longitude ( $\lambda$ ) grid points. The latitude dependence is shown  
 9 explicitly here, since we will examine errors as a function of latitude in Section 4. The  
 10 percentage difference in vector wind error relative to the initial error is then calculated,

$$V_{DIFF}(\varphi, t) = \left[ \frac{V_{RMSE}(\varphi, 0) - V_{RMSE}(\varphi, t)}{V_{RMSE}(\varphi, 0)} \right] \times 100\%, \quad (9)$$

11 and WEP is defined as the area-weighted global average of this quantity, calculated using-

$$12 \quad \text{WEP}(t) = \frac{\sum_{\varphi} V_{DIFF}(\varphi, t) \cos \varphi}{\sum_{\varphi} \cos \varphi}, \quad \text{where the summation is over all latitudes.}$$

13  
 14 A WEP value of 100% indicates the analysis equals the truth (i.e.,  $V_{RMSE}(\varphi, t) = 0$ ). Although  
 15 WEP is relative to the initial error, and therefore will vary from one experiment design to  
 16 another, it provides a useful normalized number for quantitative comparison between runs using  
 17 the same initial error. In this paper, all experiments start with the same initial vector wind error  
 18 with a global mean ~~(indicated by tilde)~~ value,  $\tilde{V}_{RMSE}(0) = 4.55 \text{ m s}^{-1}$ , so WEP can be compared  
 19 directly among all runs (here the tilde is used to refer to the global area-weighted mean). As a  
 20 rule of thumb, an approximate conversion from WEP to wind component error can be derived by  
 21 assuming RMS wind errors do not vary with latitude and assuming zonal and meridional wind  
 22 errors are equal. Using Eqs. (8) and (9), this results in the following approximation

$$\tilde{u}_{RMSE}(t) = \tilde{u}_{RMSE}(0) \times [1 - \text{WEP}(t)/100]. \quad (10)$$

1 The initial global mean zonal wind RMSE,  $\tilde{u}_{RMSE}(0)$ , is  $\sim 3.3 \text{ m s}^{-1}$ , so WEP values of 50, 60, 70,  
 2 80, and 90 correspond to approximate wind component errors of 1.65, 1.30, 1.00, 0.66, and 0.33  
 3  $\text{m s}^{-1}$ , respectively.

4

5 Experiment errors are generally presented as the “final” error of the 10 d simulations. To reduce  
 6 random noise, the final errors are calculated as the average values over the last day of each 10-d  
 7 simulation. To estimate the statistical uncertainty in the final errors, Experiment 3 was repeated  
 8 ten times with different random observation perturbations, with a localization of 3500 km. The  
 9 standard deviation of the final values was  $\sim 0.5\%$  for WEP,  $\sim 0.02 \text{ m s}^{-1}$  for the wind components,  
 10  $\sim 0.4 \text{ m}$  for height, and  $\sim 0.002 \text{ ppmv}$  for ozone. The results in Table 1 are presented with the  
 11 number of significant digits that reflect the uncertainties determined from this test.

12

13 The final diagnostic is designed to measure the amount of gravity wave “noise” in the system,  
 14 also called “imbalance.” Imbalance is defined here using the uninitialized height  $z_{uninit}$  and  
 15 initialized height  $z_{init}$  (i.e., after NMI has been applied). As with WEP, we first calculate the  
 16 RMS difference between these two fields as a function of latitude

17

$$z_{RMS}(\varphi, t) = \sqrt{\sum_{\lambda} [z_{uninit}(\lambda, \varphi, t) - z_{init}(\lambda, \varphi, t)]^2 / \text{NLON}}. \quad (11)$$

18 ~~where NLON is the number of longitude grids and the summation is over all longitudes,~~ and then  
 19 we calculate the area-weighted global mean, ~~where the summation is over all latitudes.~~

$$\text{Imbalance}(t) = \sum_{\varphi} z_{RMS}(\varphi, t) \cos \varphi / \sum_{\varphi} \cos \varphi \quad (12)$$

20 We note here that the TR used in this paper contains negligible gravity wave amplitudes at  
 21 frequencies higher than  $1.0 \text{ day}^{-1}$ . The imbalance calculated by applying NMI to the TR is less  
 22 than 1 m. So any imbalance greater than  $\sim 1 \text{ m}$  is due to spurious GW generation.

## 1 4. Results and discussion

### 2 4.1 Experiment 1: Ozone only

3 In this section, we examine the performance of the  $\text{SWM}^{\text{T}}$ -EnKF system when ozone data are  
4 assimilated alone. Figure 7 shows time series of error diagnostics for the two “optimal” runs  
5 from Experiment 1 (tuning of the covariance localization to determine the optimal run is  
6 described later in this section). Results are presented both for uninitialized (solid lines) and  
7 initialized (NMI, dotted lines) output. The uninitialized WEP steadily increases before leveling  
8 off at final values of  $\sim 46\%$  for EnKF- $uv$  and  $\sim 58\%$  for EnKF- $\psi\chi$ , with corresponding wind  
9 component errors of  $\sim 1.6 \text{ m s}^{-1}$  and  $\sim 1.3 \text{ m s}^{-1}$ . Most of the improvement occurs during the first  
10 five days. After applying NMI to these runs, the initialized WEP increases significantly for both  
11 systems, indicating that imbalance is limiting the wind improvement and error reduction.

12  
13 The uninitialized height error for EnKF- $uv$  levels out at  $\sim 61 \text{ m}$ , while for EnKF- $\psi\chi$ , the  
14 uninitialized height error reaches  $\sim 43 \text{ m}$ . Much of the height error can be attributed to GW  
15 generated in the system. Figure 7e shows that the imbalance starts near zero, but increases as  
16 GW are introduced into the system. For EnKF- $uv$ , the imbalance rises rapidly over the first two  
17 days until it nearly matches the uninitialized height error. After this time, the further growth of  
18 GW is likely restrained by the weak dissipation in the  $\text{SWM}^{\text{T}}$  system. For EnKF- $\psi\chi$ , the  
19 imbalance grows more slowly, but is still close to the uninitialized height error at the end.  
20 Because the uninitialized height error and imbalance are still increasing at the end of 10 days,  
21 this suggests that the GW have not saturated for EnKF- $\psi\chi$ . Application of NMI results in  
22 dramatically reduced height errors for both systems. There is an  $\sim 1$  day oscillation in the  
23 initialized height errors, which is largely due to the one traveling eastward GW mode that is not  
24 initialized, which is present in the TR. The decreasing amplitude of the oscillation with time  
25 suggests that this mode is being resolved by the system through the ozone-wind extraction.

26  
27 The ozone errors (Fig. 7f) show a sharp decrease over the first day, followed by a gradual  
28 decline. Although the errors in the dynamical variables have leveled out by day 10, the ozone  
29 errors appear to still be declining. Both runs show final ozone errors less than the observation  
30 error of  $0.08 \text{ ppmv}$ . As a global consistency check of the EnKF solution, we also calculated

1  $\overline{\chi^2} = \overline{\mathbf{d}}^T [\mathbf{H}\mathbf{P}_{ens}^b \mathbf{H}^T + \mathbf{R}]^{-1} \overline{\mathbf{d}} \times (\text{NOBS})^{-1}$ , where  $\overline{\mathbf{d}}$  is the ensemble mean innovation and NOBS is  
2 the number of observations. For a well-tuned system, this “chi-squared” diagnostic should equal  
3 ~~the number of observations~~one (Ménard et al., 2000). Since the SPREAD is tuned to match a  
4 subset of the elements of the state vector rather than the entire state vector, we don’t expect ~~the~~  
5 ~~normalized~~  $\overline{\chi^2}$  to be exactly unityone, but it should be relatively close, at least in the time-  
6 average. For these experiments,  $\overline{\chi^2}$  (not shown) starts out slightly high, but levels out to a time-  
7 mean (averaged from 2-10 d) of 0.99 for EnKF-*uv* and 0.97 for EnKF- $\psi\chi$ .

8  
9 In Fig. 8, the analysis errors are projected onto the GW and RW modes. As expected from the  
10 imbalance calculations, the uninitialized EnKF-*uv* has much larger GW error due to larger  
11 imbalance in the increments. However, the EnKF-*uv* has slightly smaller RW errors. This is  
12 consistent with the initialized EnKF-*uv* having slightly larger WEP than the initialized EnKF- $\psi\chi$   
13 (Fig. 7a). This difference may be partly due to background error estimation biases caused by the  
14  $\psi\chi$ -localization, as discussed in Kepert (2009). These biases will either overweight or  
15 underweight the background at different scales, resulting in a suboptimal solution. We could try  
16 to correct for this effect by altering the observation error covariance as in Kepert (2009), but this  
17 does not account for the scale dependence of the bias. The situation in our case is also  
18 complicated by the adaptive inflation, which uses different state variables in EnKF-*uv* and  
19 EnKF- $\psi\chi$ .

20  
21 Figure 9 (column 1) presents several global error diagnostics versus localization length for  
22 Experiment 1. We define the “optimal” runs for each experiment as those that maximize WEP.  
23 These are indicated by squares (triangles) for uninitialized (initialized) results in Fig. 9a and are  
24 also listed in Table 1. In Fig. 9a,b the uninitialized WEP and zonal wind errors (meridional wind  
25 errors are very similar and are not shown) exhibit strong dependence on L, with maximum WEP  
26 occurring at L = 1500 km for EnKF-*uv* and L = 2500 km for EnKF- $\psi\chi$ . The optimal EnKF- $\psi\chi$   
27 run results in larger WEP and smaller wind error compared EnKF-*uv*, which would appear to  
28 favor the choice of  $\psi\chi$  or *uv*. However, EnKF- $\psi\chi$  is much more ~~sensitivity~~ sensitive to  
29 variations in L, with WEP values actually becoming negative at small and large L.

1  
2 Figure 9c shows a height error minimum at  $L = 2000$  km for uninitialized EnKF- $\psi\chi$ , while for  
3 uninitialized EnKF- $uv$  the height error increases monotonically with  $L$ . The increase of height  
4 error with  $L$  is driven by the increase of imbalance with  $L$ , as seen in Fig. 9d. This increase in  
5 imbalance with longer  $L$  when assimilating only ozone observations is a new finding, which is  
6 opposite to the tendency of localization to create imbalance when assimilating dynamical  
7 observations, as will be shown in our Experiment 2 and discussed by Mitchell et al. (2002) and  
8 Kepert et al. (2009, 2011). It is likely that ozone observations cause increased imbalance with  $L$   
9 due to spurious ensemble correlation between ozone and the dynamical variables at large  
10 distances, which are projected onto the gravity modes. ~~Over most of the range of localizations~~ Up  
11 ~~to 4000 km~~, the EnKF- $uv$  has larger imbalance than EnKF- $\psi\chi$ , which is consistent with the  
12 single-observation simulations. The ozone errors (Fig. 9e) show a broad minimum, with the  
13 EnKF- $uv$  providing slightly better values at all  $L$ .

14  
15 After application of NMI, for both EnKF- $uv$  and EnKF- $\psi\chi$  the wind and height errors are  
16 smaller and WEP is larger at all values of  $L$ . The ozone error does not change, since the NMI is  
17 applied only to the dynamical fields. The initialized results show WEP maximizing at  $\sim 84\%$  for  
18 EnKF- $uv$  and  $\sim 81\%$  for EnKF- $\psi\chi$  (see ~~squares—triangles~~ on Fig. 9a). The length scales  
19 corresponding to these values increase to 2000 km for EnKF- $uv$  and 3500 km for EnKF- $\psi\chi$ ,  
20 suggesting the correlations at larger lengths are more reliable. That EnKF- $uv$  outperforms EnKF-  
21  $\psi\chi$  when NMI is applied is consistent with Kepert (2009), who showed that EnKF- $uv$  (with  
22 NMI) resulted in smaller height and wind errors than the EnKF- $\psi\chi$  (with NMI) due to  
23 background error estimation biases caused by the  $\psi\chi$ -localization.

24  
25 Up to this point, we have examined globally-averaged analysis errors. To determine regional  
26 impact, we also examine how the errors vary with latitude for Experiment 1, shown in Fig. 10  
27 (column 1). The initial wind errors (black lines in Fig. 10a,b) are largest in the NH tropics and  
28 midlatitudes and near the North Pole (global maps of initial wind and height errors are provided  
29 in Fig. 3 of Allen et al. (2014)). After assimilating ozone, the uninitialized wind errors are  
30 reduced at most latitudes. Small increases in uninitialized zonal wind error occur near  $70^\circ\text{S}$  and

1 70°N. That the tropical bias has been removed is important, since the tropical winds are not as  
2 well constrained in the stratosphere by radiance observations alone. The uninitialized height  
3 errors (Fig. 10c) are more uniform after ozone assimilation, and show slight improvement in  
4 some regions. However, uninitialized height errors have also increased over large portions of the  
5 globe, particularly for EnKF- $uv$ . This is due largely to the imbalance generated by the ozone  
6 observations. Results with NMI (dotted lines on Fig. 10a,b,c) show reduced height (and wind)  
7 errors at all latitudes compared to the original analyses, due to removal of spurious GW. Ozone  
8 errors (Fig. 10d) are also reduced at all latitudes in this ozone assimilation  
9 Experiment~~experiment~~, with slightly larger errors in the tropics.

#### 10 4.2 Experiment 2: Height only

11 We now examine the results of Experiment 2, when only height data are assimilated. For both  
12 EnKF- $uv$  and EnKF- $\psi\chi$ , Fig. 9 (column 2) shows that WEP initially increases and wind errors  
13 decrease with less localization (larger L), with optimal values occurring at L = 5000 km for  
14 EnKF- $uv$  and L = 7000 km for EnKF- $\psi\chi$ , followed by a slight degradation at larger lengths. The  
15 EnKF- $\psi\chi$  generally performs ~~slightly~~ better than EnKF- $uv$ . The minimum wind errors are ~1.3  
16 m s<sup>-1</sup> for EnKF- $uv$  and 1.0 m s<sup>-1</sup> for EnKF- $\psi\chi$ , which are reasonable values for a well-  
17 constrained stratospheric analysis. For example, Hertzog et al. (2004) compared NH  
18 stratospheric analyses with observations from long-duration balloon flights and calculated error  
19 standard deviations of the zonal wind components of ~1.3 m s<sup>-1</sup> for ECMWF and ~1.9 m s<sup>-1</sup> for  
20 National Centers for Environmental Prediction, when the observations were low-pass filtered to  
21 remove the variance due to inertia-gravity waves.

22  
23 The most striking difference between Experiments 1 and 2 is that assimilation of height  
24 observations results in much less imbalance (note different vertical scales in Fig. 9d and 9i). The  
25 imbalance, like the wind and height errors, generally decreases with less localization, which is  
26 opposite to what occurred in Experiment 1. However, this is consistent with previous studies that  
27 have examined balance in the EnKF in the context of assimilation of dynamical variables (e.g.,  
28 Mitchell et al., 2002). This result provides a caution that while reducing the localization may  
29 reduce imbalance for some observations, it may increase imbalance when assimilating ozone.

1 Applying NMI to the analyses results in almost no change to the WEP and wind errors, but does  
2 improve the height errors, particularly for EnKF- $uv$ .

3  
4 The errors as a function of latitude for Experiment 2 are shown in Figure 10 (column 2). The  
5 wind errors (Fig. 10e,f) are largest in the tropics and decrease towards the poles. This is  
6 expected, since the height is more strongly correlated with wind in the extratropics due to  
7 geostrophic balance. In the tropics this balance breaks down, and it is more difficult for the  
8 EnKF to correct the winds with height observations alone. The analyzed height errors (Fig. 10g)  
9 are markedly reduced from the initial errors, with slightly larger values in the **extratropics**.  
10 Experiment 2 also improves the ozone, but only by a small amount (Fig. 10h). The small ozone  
11 improvement is in the extratropics, likely due to more accurate winds that drive ozone advection.

#### 12 4.3 Experiment 3: Ozone and height

13 The final experiment examines the value of adding ozone assimilation to the analyses produced  
14 by the height only assimilation. The results as a function of  $L$  are shown in Fig. 9 (column 3).  
15 Not surprisingly, the additional data provided in this experiment results in the smallest errors and  
16 highest WEP values, confirming that ozone and height observations provide complimentary  
17 information to the DA system. Large WEP values occur for a broad range of  $L$ , indicating that  
18 the results are not very sensitive to the choice of localization length. The lowest uninitialized  
19 wind errors occur at  $L = 3500$  km for both EnKF- $uv$  and EnKF- $\psi\chi$  and the maximum  
20 uninitialized WEP (~87%) is larger than when either ozone or height are assimilated separately.  
21 The application of NMI slightly increases the optimal WEP to ~90% for both systems.

22  
23 The uninitialized height error and imbalance for Experiment 3 (Fig. 9m,n) show broad minima,  
24 which reflects the combined tendencies of the height observations to increase imbalance at small  
25  $L$  and the ozone observations to increase imbalance at large  $L$ . The imbalance remains relatively  
26 low in these experiments (~~←(less than 30-20 m for  $L < 5000$  km)~~), with the EnKF- $uv$  showing  
27 somewhat higher values than EnKF- $\psi\chi$ . The error in initialized height (dashed lines of Fig. 9m)  
28 does show a significant decrease, suggesting that there is some GW noise in Experiment 3, but it  
29 is much less than when ozone is assimilated alone. It appears that combining height observations  
30 with ozone observations ~~acts as a filter to dampen~~**reduces** the GW that would otherwise be



1 | generated by the ozone observations alone. ~~This suggests that the ozone assimilation is still~~  
2 | ~~exciting some GW, but the impact on wind error is very much reduced when assimilating~~  
3 | ~~heights.~~

4 |  
5 | The errors as a function of latitude for the optimal results from Experiment 3 are presented in  
6 | Fig. 10 (column 3). Wind errors are quite small ( $< 0.5 \text{ m s}^{-1}$ ) across the globe, with the primary  
7 | benefit occurring in the tropics, where wind errors are much less than either Experiment 1 or 2.  
8 | The ozone in Experiment 3 is also better than Experiment 1. Having a better background ozone  
9 | field (due to better winds) allows more efficient use of the ozone observations. This likely  
10 | provides a positive feedback in the system that enhances the ozone impact. The addition of ozone  
11 | also tends to flatten height errors with latitude. Application of NMI does not impact the wind  
12 | errors very much, but does reduce the height errors as seen in Fig. 10k.

13 |  
14 | Additional experiments (not shown) were performed with a much smaller height error standard  
15 | deviation of 10 m. Decreasing the height error for height-only assimilation increased the  
16 | maximum WEP to 84% for EnKF- $uv$  and 89% for EnKF- $\psi\chi$ . The impact of adding ozone  
17 | assimilation in these experiments was also positive, increasing the maximum WEP to 92% for  
18 | EnKF- $uv$  and 91% for EnKF- $\psi\chi$ , with most of the wind improvements occurring in the tropics.  
19 | These results suggest that even in a very well-tuned system, high quality ozone observations can,  
20 | in principle, further improve the winds.

## 21 | **5. Conclusions**

22 |  
23 | The EnKF DA is able to employ cross-correlations between state variables in the ensemble  
24 | background states to couple tracer and dynamical variables. This study examined several aspects  
25 | of extraction of wind information from EnKF ozone assimilation using an SWM coupled with  
26 | ozone advection. Three sets of experiments were performed that assimilated ozone, geopotential  
27 | height, or both. Modest improvements to the winds were observed when either ozone or height  
28 | were assimilated separately. Final WEP values of 46% (58%) were obtained for ozone and 60%  
29 | (~~67~~69%) for height with the EnKF- $uv$  (EnKF- $\psi\chi$ ) system. When NMI was applied to the ozone  
30 | experiment, WEP jumped to 84% (81%), showing that gravity wave noise was generating

1 significant error. NMI applied to the height experiment resulted in WEP increases of less than  
2 1%, suggesting very small imbalance.

3  
4 When assimilating both ozone and height, WEP rose to ~87% for both systems. Imbalance was  
5 also much less than when ozone was assimilated alone. The addition of height observations  
6 appears to provided a form of GW filtering reduce the gravity wave noise in the EnKF DA,  
7 thereby greatly reducing the need for initialization. This is important, since over-filtering could  
8 be a problem if NMI is applied to the upper stratosphere/mesosphere (Sankey et al., 2007) and  
9 the tropics (Nezlin et al., 2009), where unbalanced modes play an important role in the real  
10 atmosphere (see also Koshyk et al., 1999). Applying NMI to the combined experiment resulted  
11 in a modest increase in WEP to ~90%. The greatest impact of ozone assimilation on the winds  
12 was found to occur in the tropics, which are less well constrained by height assimilation due to  
13 lack of geostrophy.

14  
15 This study also compared results from EnKF systems that used different flow variables. While  
16 the EnKF- $uv$  system with ozone observations generated greater imbalance, this system was also  
17 able to more accurately determine the wind structure of the rotational wave modes. This may be  
18 due to biases in the specification of the background error covariance in the ENKF- $\psi\chi$ , as  
19 discussed by Kepert (2009). As a result, when NMI was applied, the EnKF- $uv$  performed slightly  
20 better than the EnKF- $\psi\chi$ . For height assimilation, the EnKF- $\psi\chi$  performed better, due to less  
21 imbalance, while the combined assimilation of ozone and height produced similar results in the  
22 two systems.

23  
24 In each experiment the localization length was tuned to maximize the wind extraction. Previous  
25 studies have shown that tighter localization increases imbalance, which may be detrimental. We  
26 showed that while this was the case for height observations, for ozone observations the imbalance  
27 actually increased with localization length. The cause is uncertain, but may be due to spurious  
28 long-range correlations between ozone and the dynamical fields, which projects onto the gravity  
29 modes of the SWM.

30

1 While under the ideal conditions used in this study WEP values of up to ~90% were achieved  
2 (wind component errors  $\sim 0.3 \text{ m s}^{-1}$ ), there are many challenges to demonstrating that the ozone-  
3 wind coupling in operational DA systems is, or can be, beneficial. There are observation system  
4 challenges such as frequency, latency, precision, and bias. There are also modeling challenges  
5 such as accurate ozone transport, chemistry, and radiation. The results here were obtained with a  
6 single-layer model, relatively low resolution (T42), and a rather simple wave-forcing scenario.  
7 Given these caveats, this study demonstrated ozone-wind interaction in the EnKF and the  
8 potential for ozone assimilation to benefit the wind analysis, particularly in the tropics.

9  
10 Whether 4D-Var or EnKF is better for ozone-wind extraction is still an open question. In our  
11 previous work we showed that wind extraction is feasible when assimilating globally-gridded  
12 hourly tracer data (ozone, nitrous oxide, or water vapor) within 4D-Var. Follow-up work (not  
13 presented here) indicates that ozone-wind extraction is also possible in 4D-Var assimilation of  
14 the ozone and height data used in this study. In future work, we plan to directly compare 4D-Var,  
15 EnKF, and hybrid methods for tracer-wind extraction.

## 16 **Acknowledgments**

17  
18 We would like to thank Alan Geer and one anonymous reviewer for helpful comments on the  
19 manuscript. This work was funded by the U. S. Office of Naval Research.

## 20 **References**

21 Allen, D. R., Hoppel, K. W., Nedoluha, G. E., Kuhl, D. D., Baker, N. L., Xu, L., and Rosmond,  
22 T. E.: Limitations of wind extraction from 4D-Var assimilation of ozone, Atmos. Chem. Phys.,  
23 13, 3501-3515, doi:10.5194/acp-13-3501-2013, 2013.

24 Allen, D. R., Hoppel, K. W., and Kuhl, D. D.: Wind extraction potential from 4D-Var  
25 assimilation of stratospheric O<sub>3</sub>, N<sub>2</sub>O, and H<sub>2</sub>O using a global shallow water model, Atmos.  
26 Chem. Phys., 14, 3347-3360, doi:10.5194/acp-14-3347-2014, 2014.

1 Andersson, E., E. Hólm, P. Bauer, A. Beljaars, G. A. Kelly, A. P. McNally, A. J. Simmons, J.-N.  
2 Thépaut, and Tompkins, A. M.: Analysis and forecast impact of the main humidity observing  
3 systems, *Q. J. Roy. Meteor. Soc.*, 133, 1473-1485, doi:10.1002/qj.112, 2007.

4 Andrews, D. G., Holton, J. R., and Leovy, C. B.: *Middle Atmosphere Dynamics*, Academic  
5 Press, Inc., Orlando, Florida, USA, 1987.

6 Baker, W. E., Atlas, R., Cardinali, C., Clement, A., Emmitt, G. D., Gentry, B. M., Hardesty, R.  
7 M., Källén, E., Kavaya, M. J., Langland, R., Ma, Z., Masutani, M., McCarty, W., Pierce, R. B.,  
8 Pu, Z., Riishojgaard, L. P., Ryan, J., Tucker, S., Weissmann, M., and Yoe, J. G.: Lidar-measured  
9 wind profiles: the missing link in the global observing system, *Bull. Amer. Meteor. Soc.*, 95(4),  
10 543-564, doi:10.1175/bams-d-12-00164.1, 2014.

11 Courtier P., and Talagrand, O.: Variational assimilation of meteorological observations with the  
12 direct and adjoint shallow-water equations, *Tellus*, 42A, 531-549, doi: 10.1034/j.1600-  
13 0870.1990.t01-4-00004.x, 1990.

14 ~~Daley, R., *Atmospheric Data Analysis*, Cambridge University Press, Cambridge, 1991.~~

15 Daley, R.: Estimating the wind-field from chemical-constituent observations - experiments with  
16 a one-dimensional extended Kalman filter, *Mon. Wea. Rev.*, 123, 181-198, doi: 10.1175/1520-  
17 0493(1995)123<0181:ETWFFC>2.0.CO;2, 1995.

18 Daley, R.: Recovery of the one and two dimensional windfields from chemical constituent  
19 observations using the constituent transport equation and an extended Kalman filter, *Meteorol.*  
20 *Atmos. Phys.*, 60, 119-136, 1996.

21 Dragani, R., and McNally, A. P.: Operational assimilation of ozone-sensitive infrared radiances  
22 at ECMWF, *Q. J. Roy. Meteor. Soc.*, 139, 2068-2080, doi:10.1002/qj.2106, 2013.

23 Evensen, G.: The ensemble Kalman filter: theoretical formulation and practical implementation,  
24 *Ocean Dynamics*, 53, 343-367, doi:10.1007/s10236-003-0036-9, 2003.

25 Fillion, L., Mitchell, H. L., Ritchie, H., and Staniforth, A.: The impact of a digital filter  
26 finalization technique in a global data assimilation system, *Tellus*, 47A, 304-323, doi:  
27 10.1034/j.1600-0870.1995.t01-2-00002.x, 1995.

1 Gaspari, G., and Cohn, S. E.: Construction of correlation functions in two and three dimensions,  
2 Q. J. Roy. Meteor. Soc., 125, 723-757, doi:10.1002/qj.49712555417, 1999.

3 Han, W., and McNally, A. P.: The 4D-Var assimilation of ozone-sensitive infrared radiances  
4 measured by IASI, Q. J. Roy. Meteor. Soc., 136, 2025-2037, doi:10.1002/qj.708, 2010.

5 Hertzog, A., Basdevant, C., Vial, F., and Mechoso, C. R.: The accuracy of stratospheric analyses  
6 in the northern hemisphere inferred from long-duration balloon flights, Q. J. Roy. Meteor. Soc.,  
7 130, 607-626, doi:10.1256/qj.03.76, 2004.

8 Hogan, T. F., Rosmond, T. E., and Gelaro, R., 'The NOGAPS forecast model: a technical  
9 description,' NRL Publication AD-A247 216, 218 pp. Naval Research Laboratory: Monterey,  
10 California, USA, Available at <http://www.dtic.mil/docs/citations/ADA247216>, 1992.

11 Houtekamer, P. L., and Mitchell, H. L.: Data assimilation using an ensemble Kalman filter  
12 technique, Mon. Wea. Rev., 126, 796-811, doi: 10.1175/1520-  
13 0493(1998)126<0796:Dauaek>2.0.Co;2, 1998.

14 Houtekamer, P. L., and Mitchell, H. L.: A sequential ensemble Kalman filter for atmospheric  
15 data assimilation, Mon. Wea. Rev., 129, 123-137, doi: 10.1175/1520-  
16 0493(2001)129<0123:Asekff>2.0.Co;2, 2001.

17 Jung, B.-J, Kim, S., and Jo, Y.: Representer-based variational data assimilation in a spectral  
18 element shallow water model on the cubed-sphere grid, Tellus A, 66, 24493,  
19 doi:10.3402/tellusa.v66.24493, 2014.

20 Kepert, J. D.: Covariance localisation and balance in an ensemble Kalman filter, Q. J. Roy.  
21 Meteor. Soc., 135, 1157-1176, doi:10.1002/qj.443, 2009.

22 Kepert, J. D.: Balance-aware covariance localisation for atmospheric and oceanic ensemble  
23 Kalman filters, Comput. Geosci., 15, 239-250, doi:10.1007/s10596-010-9188-0, 2011.

24 Koshyk, J. N., and Hamilton, K.: The horizontal kinetic energy spectrum and spectral budget  
25 simulated by a high-resolution troposphere-stratosphere-mesosphere GCM, J. Atmos. Sci., 58,  
26 329-348, doi:10.1175/1520-0469(2001)058<0329:Thkesa>2.0.Co;2, 2001.

27 Livesey N.J., Read, W.G., Froidevaux, L., Lambert, A., Manney, G.L., Pumphrey, H.C., Santee,  
28 M.L., Schwartz, M.J., Wang, S., Cofield, R.E., Cuddy, D.T., Fuller, R.A., Jarnot, R.F., Jiang,

1 J.H., Knosp, B.W., Stek, P.C., Wagner, P.A., and Wu, D.L.: 'Earth Observing System (EOS)  
2 Aura Microwave Limb Sounder (MLS) Version 3.3 Level 2 data quality and description  
3 document,' JPL D-33509, 162 pp., Jet Propulsion Laboratory, Pasadena, California, USA,  
4 Available at [http://mls.jpl.nasa.gov/data/v3-3\\_data\\_quality\\_document.pdf](http://mls.jpl.nasa.gov/data/v3-3_data_quality_document.pdf), 2001.

5 Lorenc, A. C.: The potential of the ensemble Kalman filter for NWP – a comparison with 4D-  
6 Var, *Q. J. Roy. Meteor. Soc.*, 129, 3183-3203, doi:10.1256/qj.02.132, 2003.

7 Machenhauer, B.: On the dynamics of gravity oscillations in a shallow water model, with  
8 applications to normal mode initialization, *Contrib. Atmos. Phys.*, 50, 253-271, 1977.

9 Ménard, R., Cohn, S. E., Chang, L.-P., and Lyster, P. M.: Assimilation of chemical tracer  
10 observations using a Kalman filter. Part I: Formulation, *Mon. Wea. Rev.*, 128, 2654-2671, doi:  
11 10.1175/1520-0493(2000)128<2654:Aoscto>2.0.Co;2, 2000.

12 Milewski, T., and Bourqui, M. S.: Assimilation of stratospheric temperature and ozone with an  
13 ensemble Kalman filter in a chemistry-climate model, *Mon. Wea. Rev.*, 139, 3389-3404,  
14 doi:10.1175/2011mwr3540.1, 2011.

15 Mitchell, H. L., and Houtekamer, P. L.: Ensemble size, balance, and model-error representation  
16 in an ensemble Kalman filter, *Mon. Wea. Rev.*, 130, 2791-2808, doi: 10.1175/1520-  
17 0493(2002)130<2791:Esbame>2.0.Co;2, 2002.

18 National Research Council: Earth Science and Applications from Space: National Imperatives  
19 for the Next Decade and Beyond, National Academy Press, Washington, DC, 428 pp., available  
20 at [http://www.nap.edu/catalog.php?record\\_id=11820](http://www.nap.edu/catalog.php?record_id=11820), 2007.

21 Neef, L. J., Polavarapu, S. M., and Shepherd, T. G.: Four-dimensional data assimilation and  
22 balanced dynamics, *J. Atmos. Sci.*, 63, 1840-1858, doi:10.1175/jas3714.1, 2006.

23 Neef, L. J., Polavarapu, S. M., and Shepherd, T. G.: A low-order model investigation of the  
24 analysis of gravity waves in the ensemble Kalman filter, *J. Atmos. Sci.*, 66, 1717-1734,  
25 doi:10.1175/2008jas2585.1, 2009.

26 Nezlin, Y., Rochon, Y. J., and Polavarapu, S.: Impact of tropospheric and stratospheric data  
27 assimilation on the mesosphere, *Tellus*, 61A, 154-159, doi:10.1111/j.1600-0870.2008.00368.x,  
28 2009.

1 Norton, W.A.: Breaking Rossby waves in a model stratosphere diagnosed by a vortex-following  
2 coordinate system and a technique for advecting material contours, *J. Atmos. Sci*, 51, 644-673,  
3 doi:10.1175/1520-0469(1994)051<0654:BRWIAM>2.0.CO;2, 1994.

4 Peubey, C., and McNally, A. P.: Characterization of the impact of geostationary clear-sky  
5 radiances on wind analyses in a 4D-Var context, *Q. J. Roy. Meteor. Soc.*, 135, 1863-1876, doi:  
6 doi:10.1002/qj.500, 2009.

7 Peuch, A., Thepaut, J. N., and Pailleux, J.: Dynamical impact of total-ozone observations in a  
8 four-dimensional variational assimilation, *Q. J. Roy. Meteor. Soc.*, 126, 1641-1659, doi:  
9 10.1002/qj.49712656605, 2000.

10 Polavarapu, S., Tanguay, M., and Fillion, L.: Four-dimensional variational data assimilation with  
11 digital filter initialization, *Mon. Wea. Rev.*, 128, 2491-2510, doi: 10.1175/1520-  
12 0493(2000)128<2491:FDVDAW>2.0.CO;2, 2000.

13 Riishøjgaard, L. P.: On four-dimensional variational assimilation of ozone data in weather-  
14 prediction models, *Q. J. Roy. Meteor. Soc.*, 122, 1545-1571, doi:10.1002/qj.49712253505, 1996.

15 Ritchie, H.: Application of the semi-Lagrangian method to a spectral model of the shallow water  
16 equations, *Mon. Wea. Rev.*, 116, 1587-1598, doi: 10.1175/1520-  
17 0493(1988)116<1587:AOTSMLM>2.0.CO;2, 1988.

18 Sankey, D., Ren, S., Polavarapu, S., Rochon, Y. J., Nezhin, Y., and Beagley, S.: Impact of data  
19 assimilation filtering methods on the mesosphere, *J. Geophys. Res.*, 112, D24104,  
20 doi:10.1029/2007JD008885, 2007.

21 Semane, N., Peuch, V. H., Pradier, S., Desroziers, G., El Amraoui, L., Brousseau, P., Massart, S.,  
22 Chapnik, B., and Peuch, A.: On the extraction of wind information from the assimilation of  
23 ozone profiles in Meteo-France 4-D-Var operational NWP suite, *Atmos. Chem. Phys.*, 9, 4855-  
24 4867, doi:10.5194/acp-9-4855-2009, 2009.

25 Stoffelen, A., Pailleux, J., Kallen, E., Vaughan, J. M., Isaksen, L., Flamant, P., Wergen, W.,  
26 Andersson, E., Schyberg, H., Culoma, A., Meynard, R., Endemann, M., and Ingmann, P.: The  
27 atmospheric dynamics mission for global wind field measurement. *Bull. Amer. Meteorol. Soc.*,  
28 86, 73-87, doi:10.1175/bams-86-1-73, 2005.

1 Waters, J. W., Read, W. G., Froidevaux, L., Jarnot, R. F., Cofield, R. E., Flower, D. A., Lau, G.  
2 K., Pickett, H. M., Santee, M. L., Wu, D. L., Boyles, M. A., Burke, J. R., Lay, R. R., Loo, M. S.,  
3 Livesey, N. J., Lungu, T. A., Manney, G. L., Nakamura, L. L., Perun, V. S., Ridenoure, B. P.,  
4 Shippony, Z., Siegel, P. H., and Thurstans, R. P.: The UARS and EOS Microwave Limb Sounder  
5 (MLS) experiments, *J. Atmos. Sci.*, 56, 194-218, doi: 10.1175/1520-  
6 0469(1999)056<0194:TUAEML>2.0.CO;2, 1999.

7 Williamson, D. L., and Temperton, C.: Normal mode initialization for a multilevel grid-point  
8 model. Part II: nonlinear aspects, *Mon. Wea. Rev.*, 109, 744-757, doi: 10.1175/1520-  
9 0493(1981)109<0744:Nmifam>2.0.Co;2, 1981.

10 World Meteorological Organization: Statement of guidance regarding how well satellite  
11 capabilities meet WMO user requirements in several application areas, WMO Satellite Rep,  
12 SAT-22, 29 pp, Available at  
13 [http://library.wmo.int/opac/index.php?lvl=notice\\_display&id=11446#.U-5jq2Pb70c](http://library.wmo.int/opac/index.php?lvl=notice_display&id=11446#.U-5jq2Pb70c), 2000.  
14



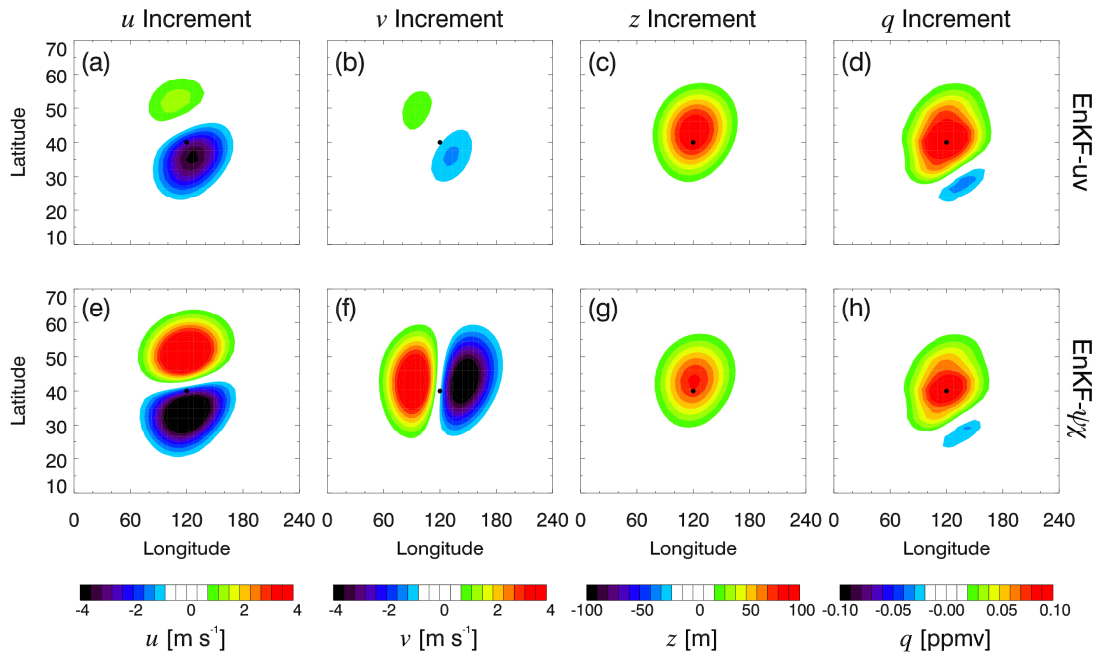
1

Experiment	L (km)	WEP (%)	$u$ error (m s <sup>-1</sup> )	$v$ error (m s <sup>-1</sup> )	$z$ error (m)	$q$ error (ppmv)
1. Ozone						
$uv$	1500	45.5	1.58	1.59	60.9	0.054
$\psi\chi$	2500	57.8	1.25	1.25	42.7	0.070
$uv$ (NMI)	2000	83.7	0.55	0.46	14.4	0.047
$\psi\chi$ (NMI)	3500	80.6	0.62	0.58	12.8	0.058
2. Height						
$uv$	5000	59.5	1.27	1.38	11.6	0.179
$\psi\chi$	<del>5000</del> 7000	<del>6668.78</del>	<del>1.030.96</del>	<del>1.131.05</del>	<del>8.47.8</del>	<del>0.151150</del>
$uv$ (NMI)	5000	60.4	1.25	1.35	6.8	0.179
$\psi\chi$ (NMI)	<del>5000</del> 7000	<del>6769.01</del>	<del>1.030.95</del>	<del>1.121.04</del>	<del>6.66.1</del>	<del>0.151150</del>
3. Both						
$uv$	3500	86.7	0.40	0.41	11.0	0.039
$\psi\chi$	3500	87.5	0.37	0.39	8.5	0.040
$uv$ (NMI)	3500	90.1	0.32	0.31	2.6	0.039
$\psi\chi$ (NMI)	4500	89.5	0.33	0.32	2.8	0.041

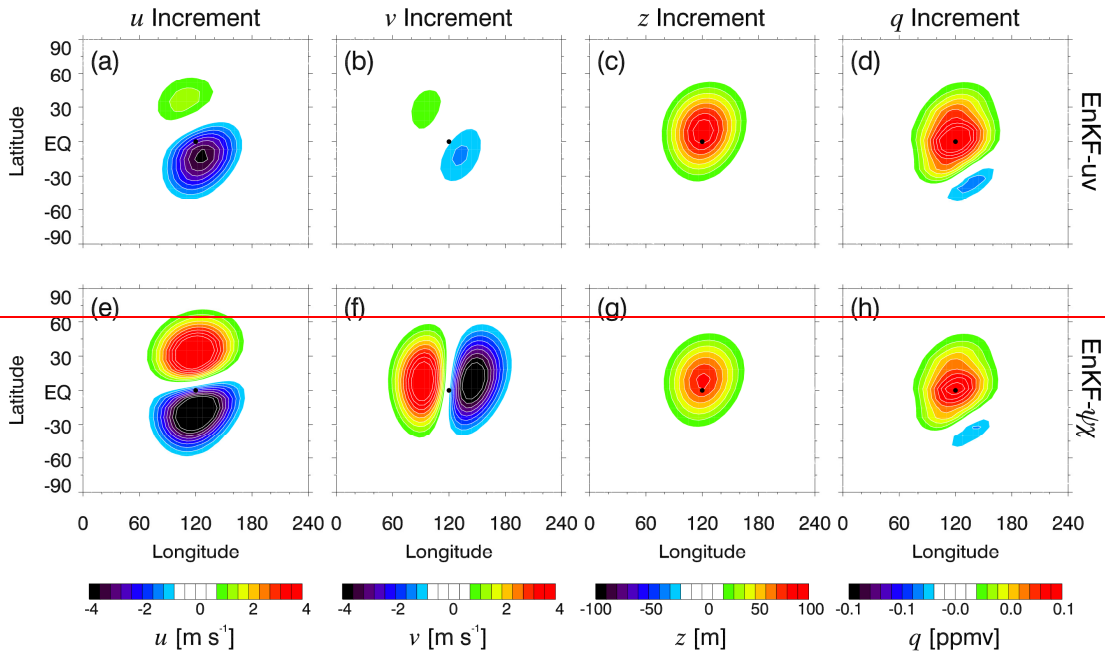
2

3 **Table 1.** Results for the optimal runs (i.e., maximum WEP) for each experiment. The  
4 localization length (L) is provided along with WEP and global mean RMSE for  $u$ ,  $v$ ,  $z$ , and  $q$ .

5



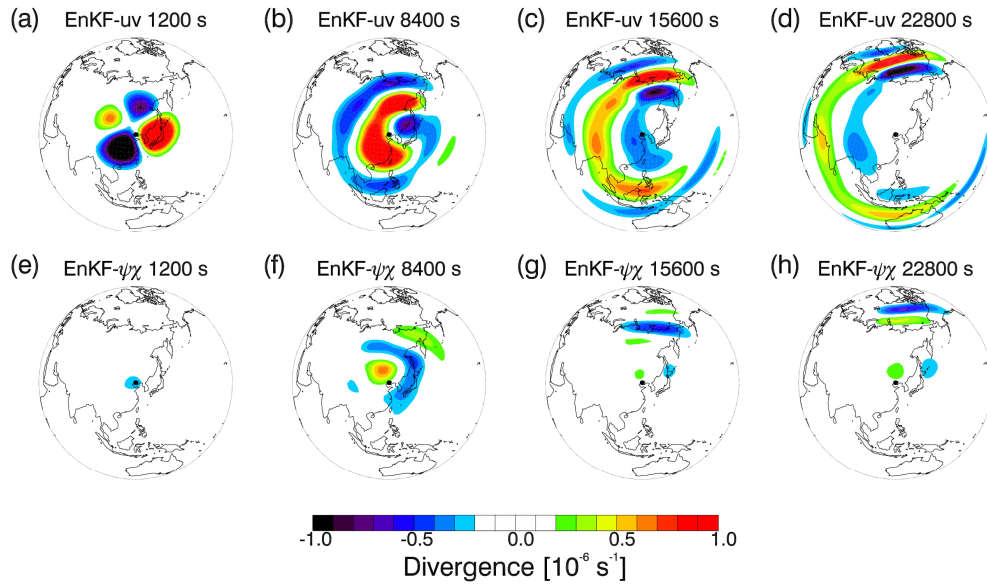
1



2

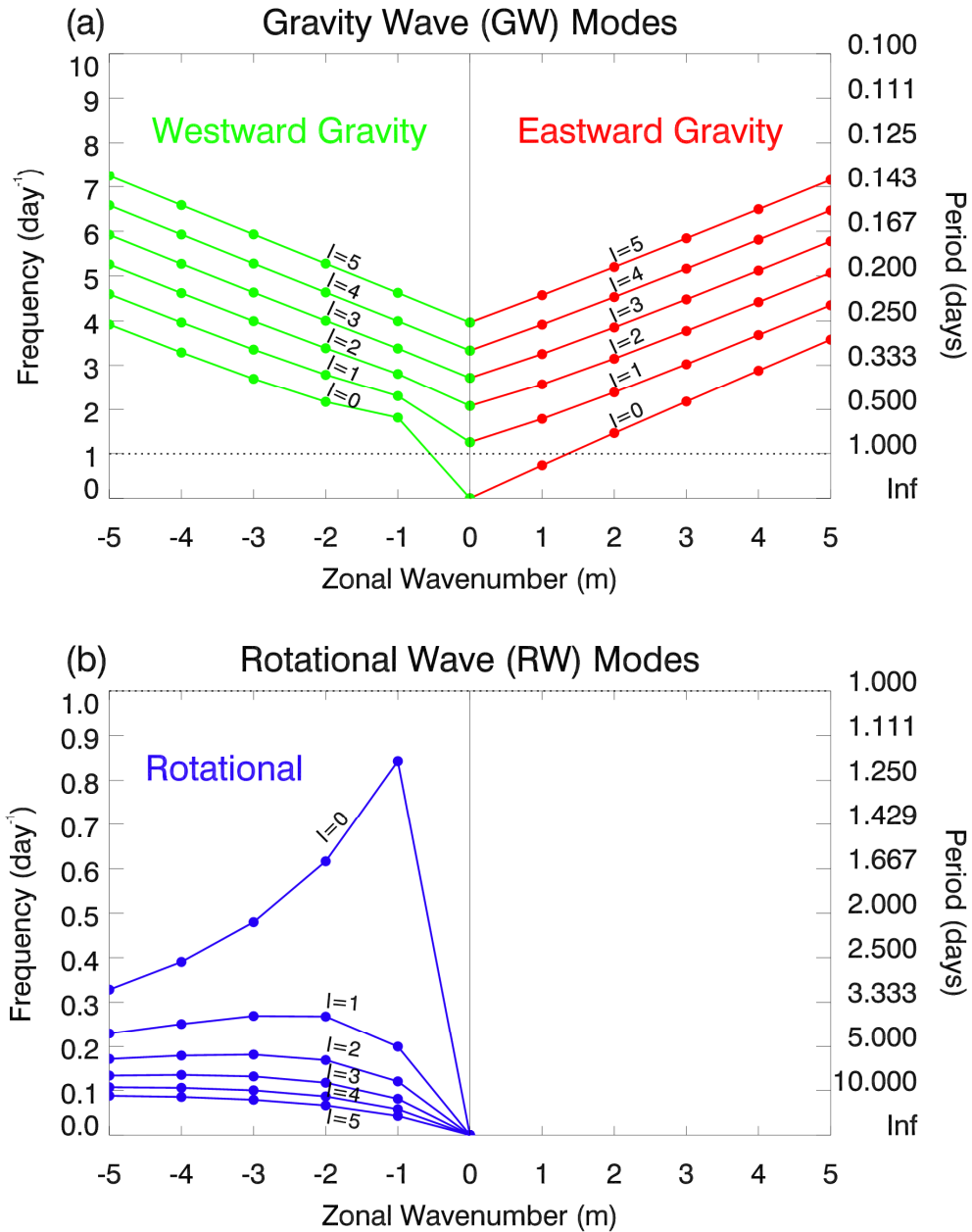
3 **Fig. 1.** Analysis increments due to assimilation of a single ozone observation (time = 1200 s) at  
 4 120°E, 40°N (indicated by black dot) using EnKF- $uv$  (top row) and EnKF- $\psi\chi$  (bottom row) with  
 5  $L = 2000$  km. Variables are given by column: zonal wind ( $u$  [ $\text{m s}^{-1}$ ], column 1), meridional wind  
 6 ( $v$  [ $\text{m s}^{-1}$ ], column 2), height ( $z$  [ $\text{m}$ ], column 3), and ozone ( $q$  [ $\text{ppmv}$ ], column 4). Red (blue)  
 7 contours indicate high (low) values for each variable.



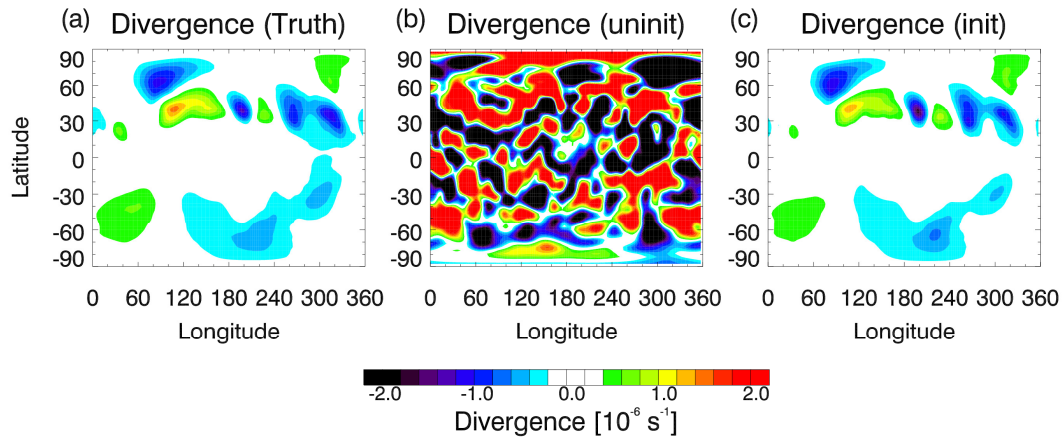


1  
 2 **Fig. 2.** Divergence anomalies [ $10^{-6} \text{ s}^{-1}$ ] due to single-observation increments (see Fig. 1) at time  
 3 = 1200 s, 8400 s, 15600 s, and 22800 s for EnKF- $uv$  (top row) and EnKF- $\psi\chi$  (bottom row). Red  
 4 (blue) contours indicate high (low) values of divergence.

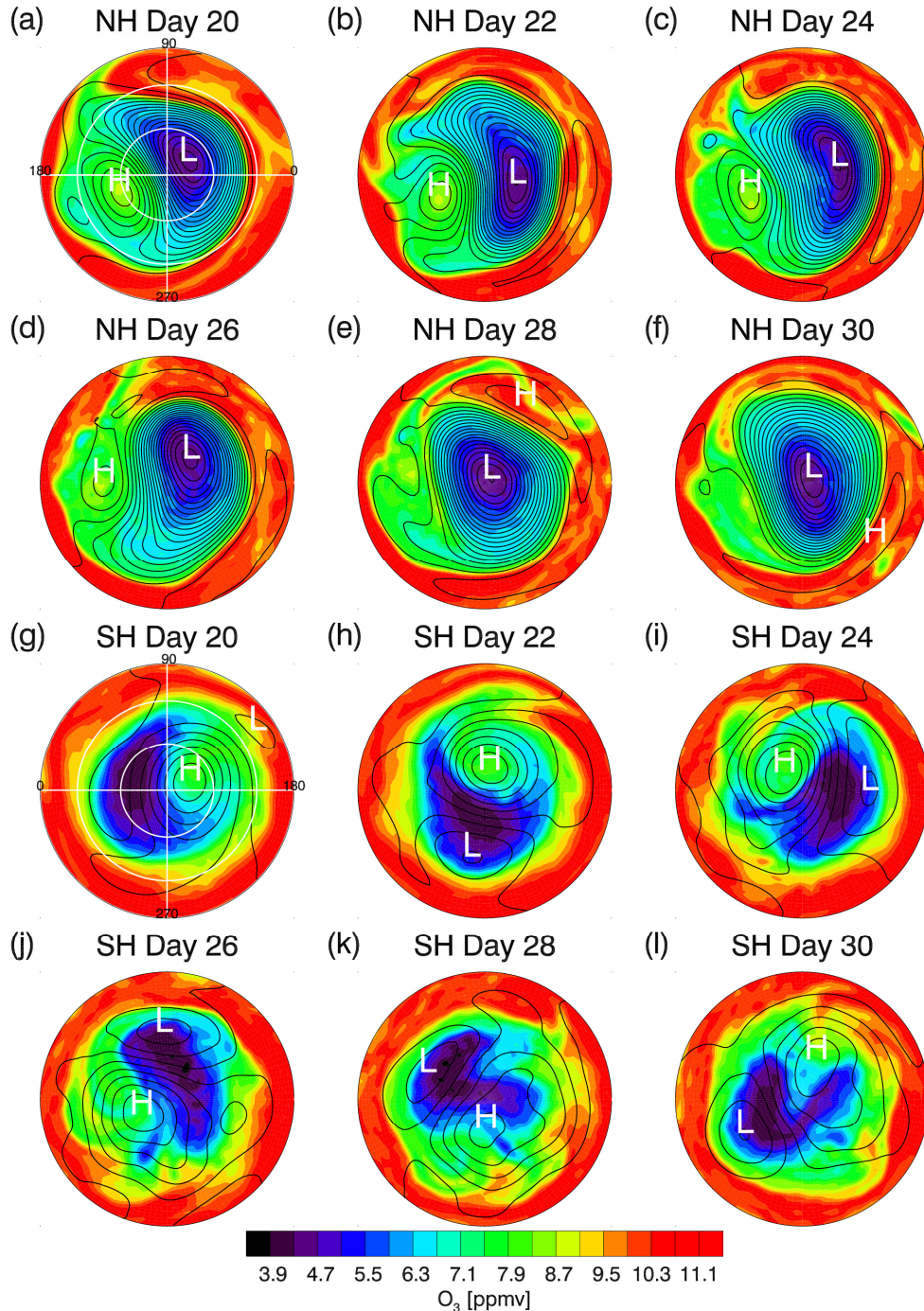
5



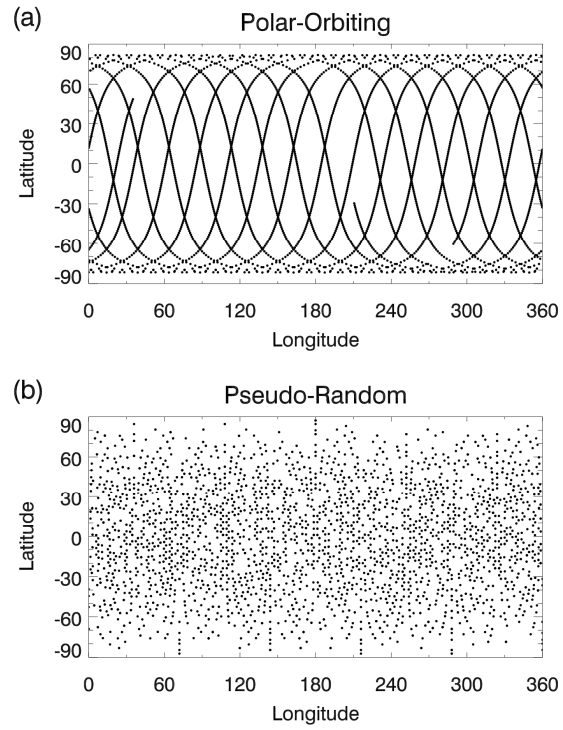
1  
2 **Fig. 3.** The normal mode frequencies [ $\text{day}^{-1}$ ] for the spectral SWM at triangular truncation T42 as  
3 a function of zonal wavenumber ( $m$ ) for the first six values of the total wavenumber  $l = m - n$ ,  
4 where  $n$  is the meridional wavenumber. Positive (negative) values of  $m$  indicate eastward  
5 (westward) motion. Modes are separated into (a) eastward and westward gravity wave (GW)  
6 modes, and (b) rotational wave (RW) modes. The cutoff frequency ( $1.0 \text{ day}^{-1}$ ) for the NMI is  
7 indicated by the dotted line. Note that the frequency scales are different for the two plots for  
8 easier viewing.



1  
 2 **Fig. 4.** Divergence [ $10^{-6} \text{ s}^{-1}$ ] maps for the (a) truth run (TR), (b) uninitialized analysis, and (c)  
 3 initialized analysis from day 2 of Experiment 1 with EnKF- $uv$  and  $L = 2000 \text{ km}$ . For each plot,  
 4 red (blue) contours indicate high (low) values.  
 5



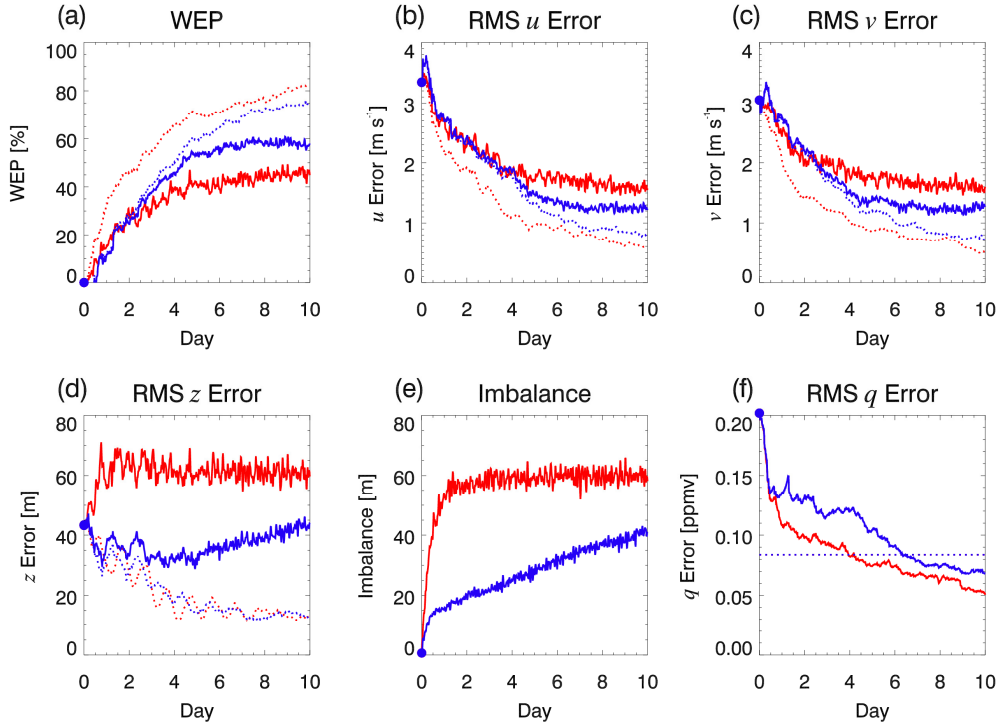
1  
 2 **Fig. 5.** Maps of ozone [ppmv] (colors) overlaid with height (black lines) at 200 m intervals for  
 3 days 20, 22, 24, 26, 28, and 30 of the truth run (TR). (a) – (f) are NH and (g) – (l) are SH. For  
 4 each plot, red (blue) contours indicate high (low) ozone values. The plots for day 20 include  
 5 longitude (latitude) grid lines at 30° (90°) intervals, with 0°, 90°, 180°, and 270° longitude  
 6 marked. The hemispheric maximum and minimum heights are indicated by “H” and “L”,  
 7 respectively.



1  
2  
3  
4

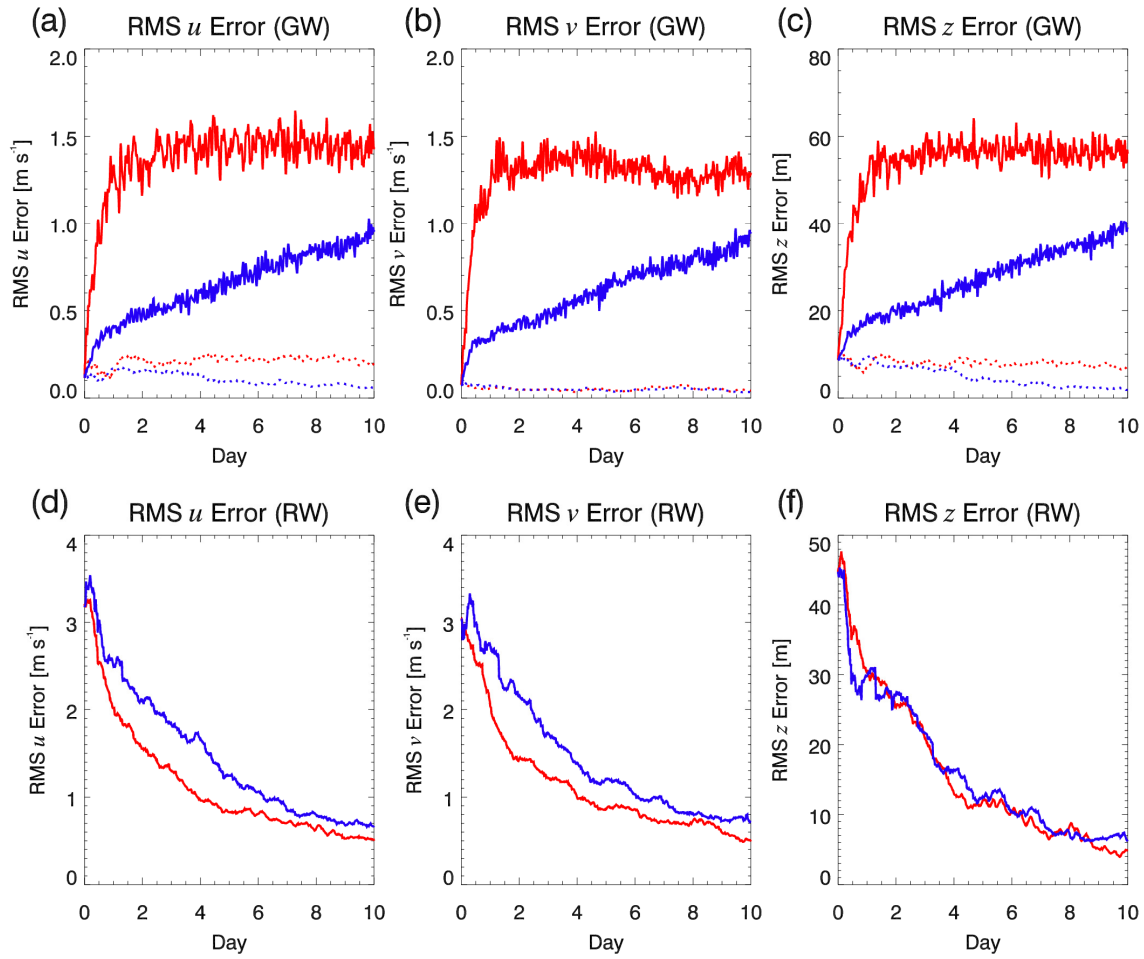
**Fig. 6.** Sampling patterns for 24 h of (a) polar-orbiting ozone data and (b) pseudo-random height data.





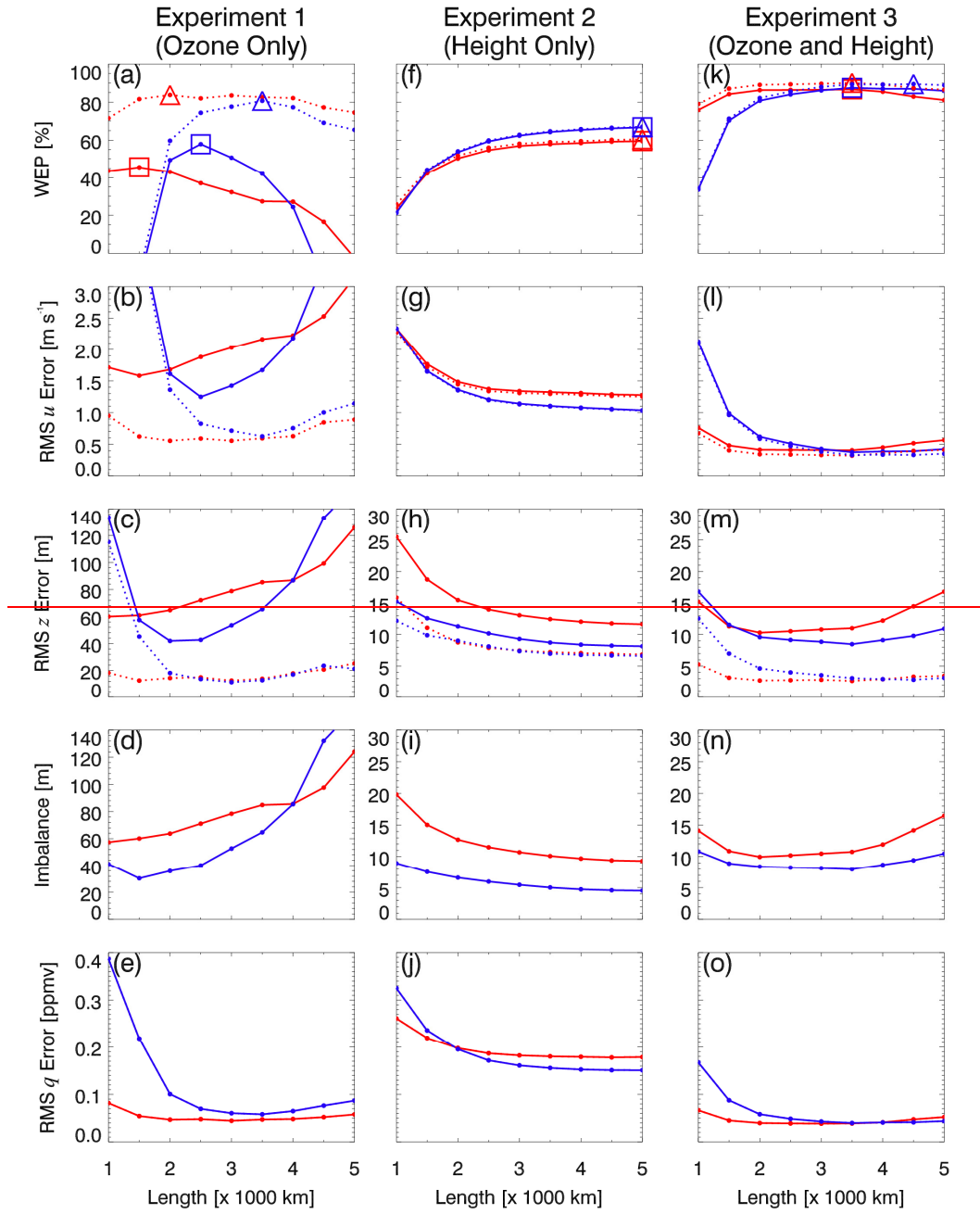
1  
2 **Fig. 7.** Diagnostics from optimal runs of Experiment 1: Ozone only ( $L = 1500$  km for EnKF- $uv$   
3 and  $L = 2500$  km for EnKF- $\psi\chi$ ). (a) WEP [%], (b), (c), and (d) RMS errors for  $u$  [ $m s^{-1}$ ],  $v$  [ $m s^{-1}$ ],  
4 and  $z$  [m], respectively, (e) Imbalance [m], and (f) RMSE for  $q$  [ppmv]. EnKF- $uv$  is red and  
5 EnKF- $\psi\chi$  is blue. Solid (dotted) lines indicate uninitialized (initialized) results (there are no  
6 dotted lines in (f) because the ozone error does not change, since the NMI is applied only to the  
7 dynamical fields). In (f) the ozone observation error standard deviation is indicated by the  
8 horizontal dotted line. Blue circles at day 0 indicate the initial values.

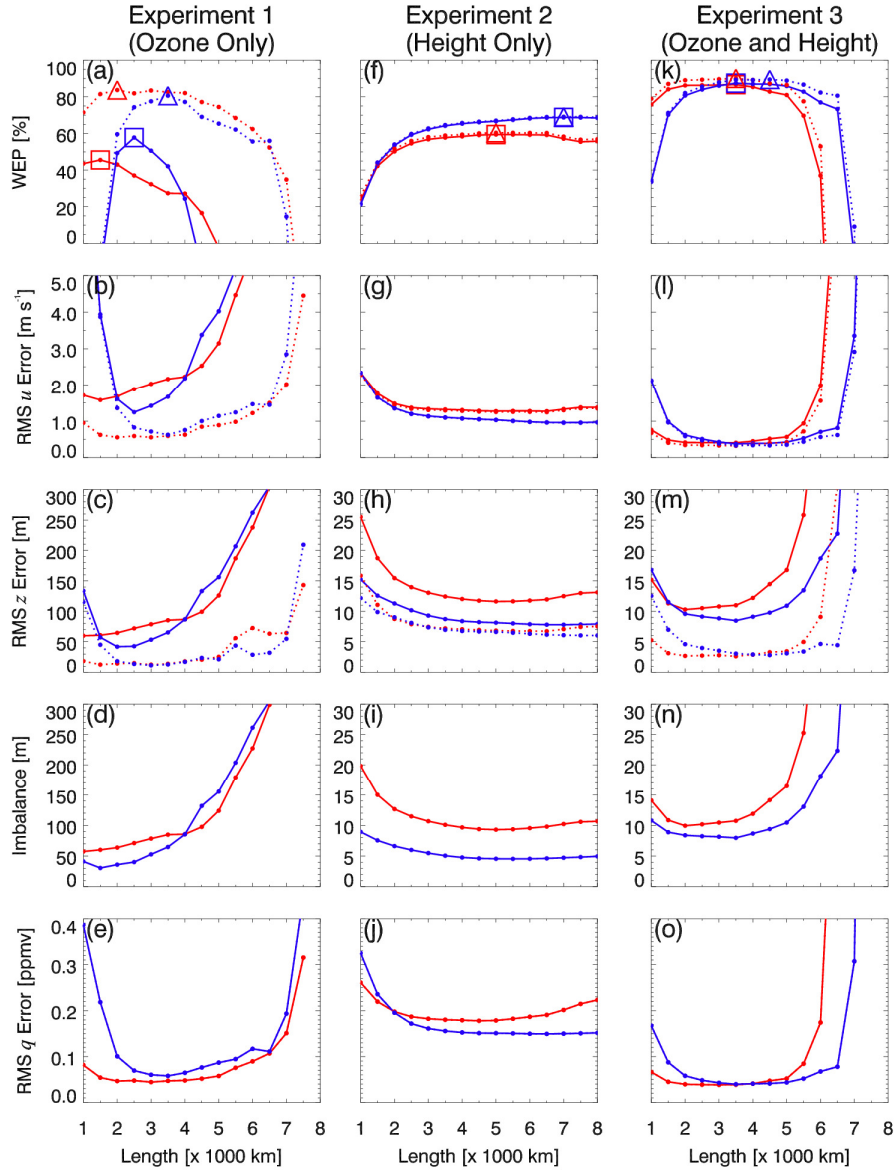
9



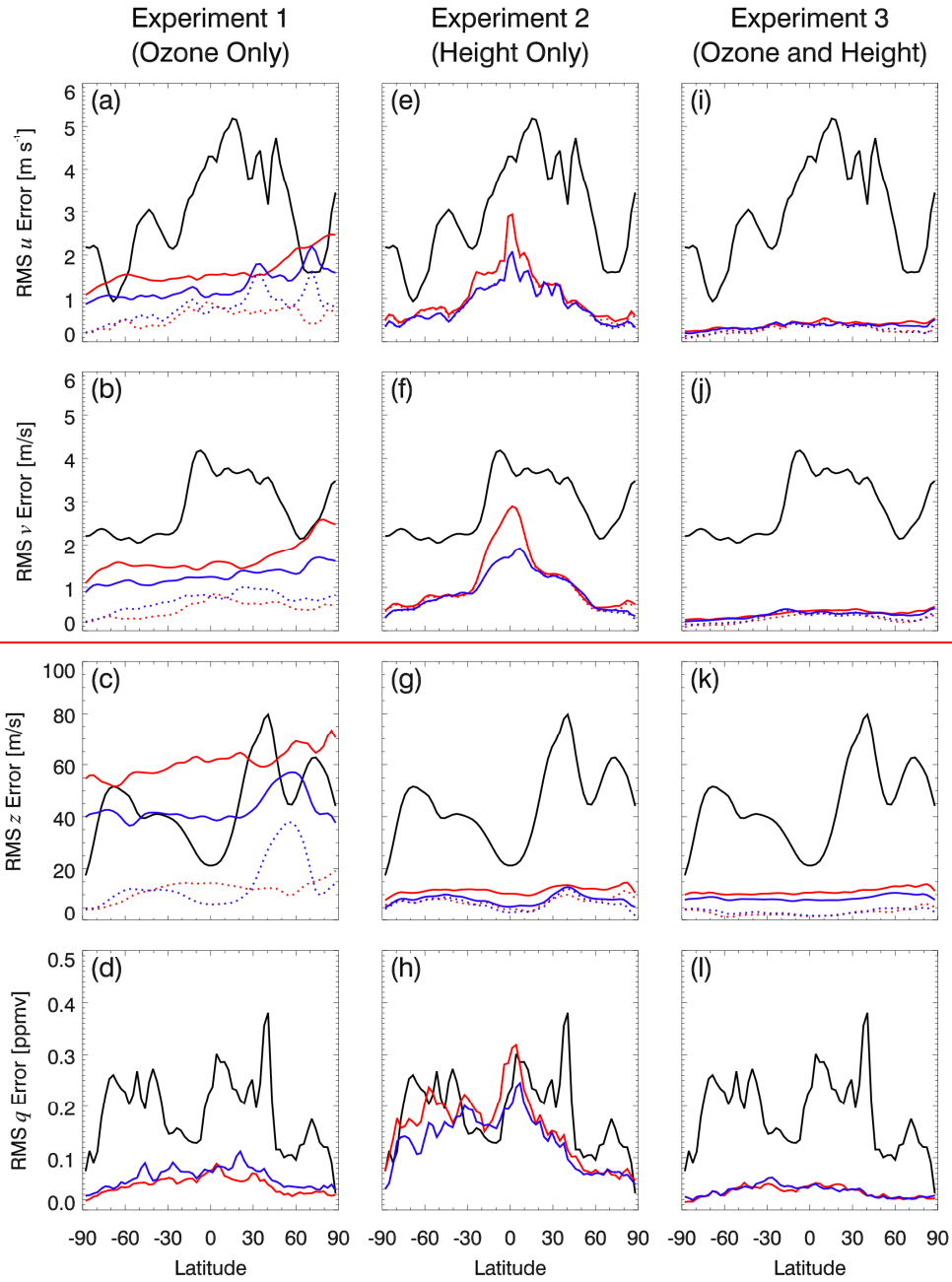
1  
 2 **Fig. 8.** RMS errors for  $u$  [m s<sup>-1</sup>],  $v$  [m s<sup>-1</sup>], and  $z$  [m] (columns 1, 2, and 3, respectively) for  
 3 gravity wave (GW) modes (row 1) and rotational wave (RW) modes (row 2) for the optimal runs  
 4 of Experiment 1: Ozone only with EnKF- $uv$  (red) and EnKF- $\psi\chi$  (blue). Solid (dotted) lines  
 5 indicate uninitialized (initialized) results.

6

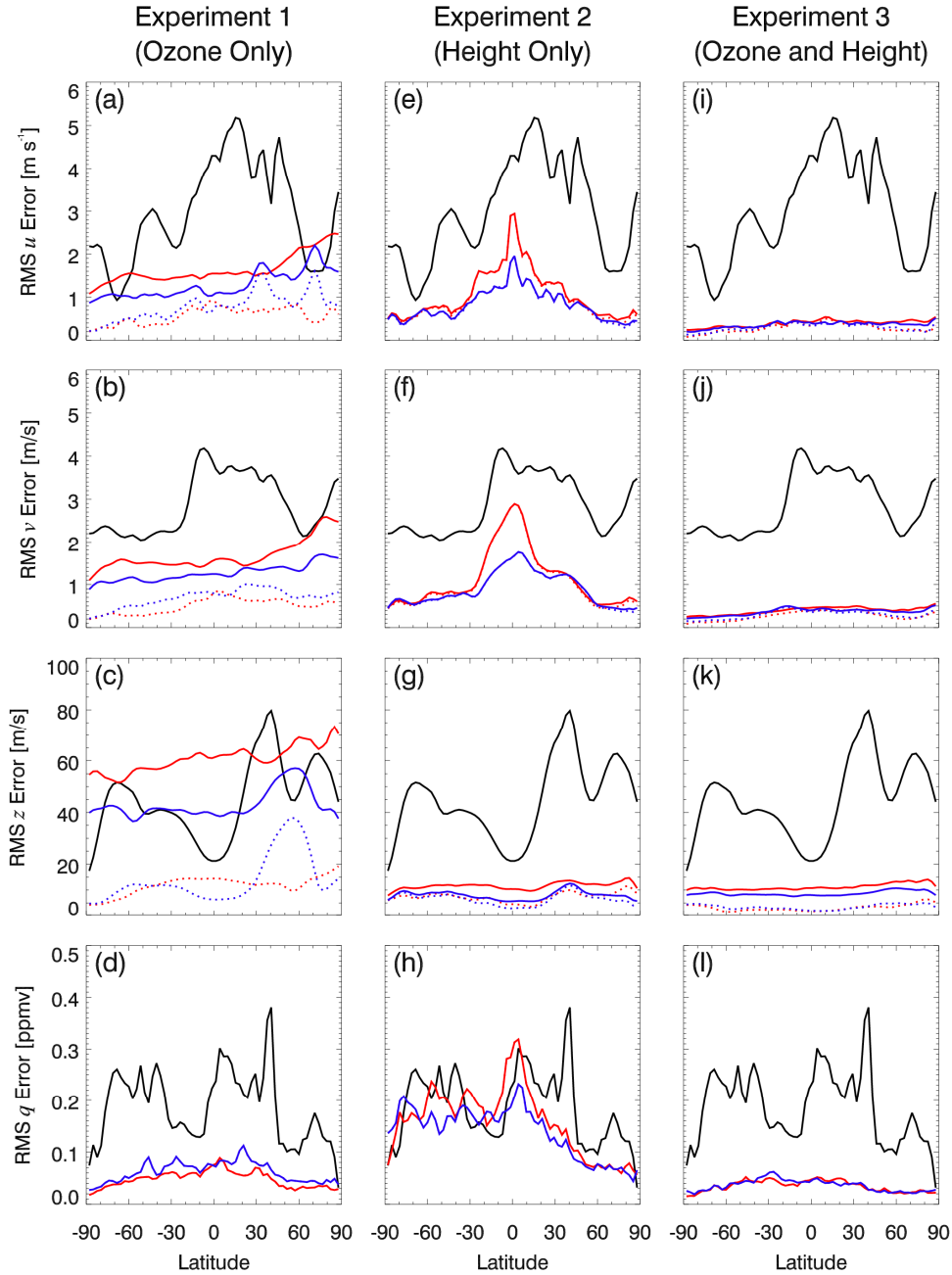




1  
2 **Fig. 9.** WEP [%] (row 1), RMS errors for  $u$  [ $\text{m s}^{-1}$ ],  $v$  [ $\text{m s}^{-1}$ ],  $z$  [m], and  $q$  [ppmv] (rows 2, 3, and  
3 5, respectively), and Imbalance [m] (row 4) as a function of localization length ( $L$ ) for  
4 Experiments 1, 2, and 3 (columns 1, 2, and 3, respectively). Red is for EnKF- $uv$  and blue is for  
5 EnKF- $\psi\chi$ . Solid (dotted) lines indicate uninitialized (initialized) results (there are no dotted  
6 lines in row 5, because the ozone error does not change, since the NMI is applied only to the  
7 dynamical fields). The optimal runs (i.e., maximum WEP) values are highlighted with squares  
8 (triangles) for uninitialized (initialized) results in row 1.



1  
2



1  
2 **Fig. 10.** RMS errors as a function of latitude for  $u$  [ $\text{m s}^{-1}$ ],  $v$  [ $\text{m s}^{-1}$ ],  $z$  [ $\text{m}$ ], and  $q$  [ $\text{ppmv}$ ] (rows 1,  
3 2, 3, and 4, respectively) for the optimal runs (as shown in Table 1 and in the highlighted squares  
4 of Fig. 9) of Experiments 1, 2, and 3 (columns 1, 2, and 3, respectively). Black lines show initial  
5 errors and red (blue) lines show EnKF- $uv$  (EnKF- $\psi\chi$ ) errors. Solid (dotted) lines indicate  
6 uninitialized (initialized) results (there are no dotted lines in (row 4) because the ozone error  
7 does not change, since the NMI is applied only to the dynamical fields).